



## Determination of the Top-Quark Mass with ATLAS Data and Complete Resonant NLO Calculations

Ludovic Scyboz





# Determination of the Top-Quark Mass with ATLAS Data and Complete Resonant NLO Calculations

Ludovic Scyboz

Vollständiger Abdruck der von der Fakultät für Physik der Technischen Universität München zur Erlangung des akademischen Grades eines

**Doktors der Naturwissenschaften (Dr. rer. nat.)**

genehmigten Dissertation.

**Vorsitzender:**

Prof. Dr. Vorname Nachname

**Prüfende der Dissertation:**

1. Prof. Dr. Vorname Nachname
2. Prof. Dr. Vorname Nachname,  
Technische Universität München

Die Dissertation wurde am 18.05.2019 bei der Technischen Universität München eingereicht und durch die Fakultät für Physik am 07.07.2019 angenommen.



## <sup>5</sup> Abstract

6 In the Standard Model (SM) of Particle Physics, the top-quark plays the role of a centre-  
7 piece. It interacts across all sectors and with all gauge fields, and has been successfully  
8 used as a portal to precision measurements of the SM. Top-quarks are also indirectly  
9 related to other SM sectors, for example to Higgs boson production processes which  
10 are induced predominantly by top-quark loops at the Large Hadron Collider (LHC).  
11 During Runs I and II of the LHC, a large number of top-quark pair ( $t\bar{t}$ ) and single-  
12 top events were recorded. They allowed to improve the experimental uncertainty on  
13 top-quark properties, like the top-quark mass, but also spin correlations and  $W$ -boson  
14 polarization in  $t\bar{t}$  events, the  $Wtb$  coupling, or flavour-changing neutral currents. In the  
15 case of the top-quark mass, the experimental uncertainties of the latest ATLAS and  
16 CMS combination are now competing with theoretical uncertainties: approximations  
17 that were previously thought to be appropriate must be reevaluated. The narrow-width  
18 approximation (NWA) for top-quark pair production in particular, which assumes the  
19 production of an on-shell top- and anti-top quark, is used in Monte-Carlo (MC) pre-  
20 dictions for most experimental analyses. Since the actual final-state is composed of  
21 the top-quark pair decay products, though, an accurate description of the signal should  
22 consider  $W^+W^-b\bar{b}$  final-states instead, which generate diagrams that do not necessarily  
23 factorize in the top-quark decay legs, nor even contain a top-quark pair to begin with.  
24 These diagrams are called non-factorizing, respectively non-doubly resonant. In cases  
25 where measurements rely on phase-space regions sensitive to these contributions, the  
26 extracted top-quark mass will be biased.

27 In this work, we take the example of the 8 TeV ATLAS top-quark mass analysis in the  
28  $e\mu$  dilepton channel, which bases on simulated templates to extract the Monte-Carlo top-  
29 quark mass by an unbinned likelihood fit. In a similar setup, we compare the extracted  
30 top-quark masses at parton-level for different theoretical descriptions of the  $t\bar{t}$  final-state  
31 at next-to-leading order (NLO) in production. In this respect, MC events are produced  
32 for three different descriptions of the top-quark decay in the NWA, as well as for the full  
33  $W^+W^-b\bar{b}$  process at NLO in production. The top-quark mass  $m_t^{\text{MC}}$  extracted by the  
34 template fit method is compared for each of these theoretical descriptions, and important  
35 biases of up to  $\Delta m_t^{\text{MC}} \sim 1 \text{ GeV}$  are underlined. A more realistic assessment, where these  
36 predictions are folded to detector-level, is also presented.

37 As mentioned, the top-quark mass also plays an important role in other sectors of the  
38 SM. With the example of di-Higgs production at LHC at 13 TeV, we show that the  
39  $m_t$  dependence of QCD NLO corrections introduces sizeable differences with respect to  
40 predictions where top-quark degrees of freedom are integrated out. A full-fledged MC  
41 event generator (with the possibility of varying the Higgs self-coupling and the Higgs-top  
42 Yukawa coupling) is introduced.



## <sup>43</sup> Zusammenfassung

<sup>44</sup> Im Standard-Modell (SM) der Teilchenphysik spielt der Top-Quark eine zentrale Rolle.  
<sup>45</sup> Er wechselwirkt mit Teilchen aller Sektoren sowie mit allen quantentheoretischen Eich-  
<sup>46</sup> feldern, und wurde in verschiedenen Kontexten als Eingangspunkt zu Präzisionsmessungen  
<sup>47</sup> des SM verwendet. Top-Quarks sind auch eng mit anderen Sektoren des SM verbun-  
<sup>48</sup> den: Higgs-Boson Produktionsprozessen zum Beispiel werden am Large Hadron Collider  
<sup>49</sup> (LHC) überwiegend durch Top-Quark-Schleifen erzeugt. Während Runs I und II des  
<sup>50</sup> LHC wurde eine massive Anzahl an Top-Quark-Paar ( $t\bar{t}$ ) und Einzel-Top-Events ermit-  
<sup>51</sup> telt. Diese haben es ermöglicht, Messungen von Top-Quark-Eigenschaften bedeutend  
<sup>52</sup> zu verbessern, beispielsweise die der Top-Quark-Masse. Im Fall der Top-Quark-Masse  
<sup>53</sup> sind die von ATLAS und CMS angegebenen experimentellen Unsicherheiten zu dem  
<sup>54</sup> Punkt gekommen, wo sie mit den aktuellen theoretischen Unsicherheiten rivalisieren:  
<sup>55</sup> das heisst insbesondere, dass früher akzeptierte Approximationen neu abgeschätzt wer-  
<sup>56</sup> den müssen. Die sogenannte Schmal-Breite-Approximation (NWA), bei der ein Top-  
<sup>57</sup> Quark-Paar on-shell produziert wird, wird üblicherweise in den meisten Monte-Carlo  
<sup>58</sup> (MC) Analysen verwendet. Weil der gemessene  $t\bar{t}$ -Endzustand aber vom endlichen Zer-  
<sup>59</sup> fallsprodukt gebildet wird, sollte eine konsistente Beschreibung des Signals eher auf dem  
<sup>60</sup> intermediären  $W^+W^-b\bar{b}$ -Zustand beruhen. Letzterer beinhaltet Feynman-Diagramme,  
<sup>61</sup> die entweder nicht in zwei faktorisierten Top-Zerfall-Kanälen kollabieren, oder überhaupt  
<sup>62</sup> keine zwei Top-Propagatoren aufweisen. Diese Diagramme heissen nicht-faktorisierend,  
<sup>63</sup> bzw. nicht-doppelt-resonant. Wenn Messungen durchgeführt werden, die sensitiv auf  
<sup>64</sup> solche Beiträge sind, kann sich ein Bias in der extrahierten Top-Quark-Masse bilden.

<sup>65</sup> Wir nehmen als Beispiel die ATLAS Top-Quark-Masse Analyse im  $e\mu$ -Dileptonkanal  
<sup>66</sup> hin, welche auf simulierten Templates basiert zum Extrahieren der Top-Quark-Masse.  
<sup>67</sup> In einem naheliegenden Setup wird die extrahierte Top-Masse verglichen, wo unter-  
<sup>68</sup> schiedliche  $t\bar{t}$ -Endzustandsbeschreibungen auf next-to-leading-order (NLO) in Produk-  
<sup>69</sup> tion eingesetzt werden. Genauer werden für drei verschiedenen Beschreibungen des Top-  
<sup>70</sup> Quark-Zerfalls, sowie für die volle NLO  $W^+W^-b\bar{b}$ -Rechnung, Verteilungen erzeugt. Die  
<sup>71</sup> mithilfe der Template-Fit-Methode extrahierte Top-Quark-Masse  $m_t^{\text{MC}}$  zeigt erhebliche  
<sup>72</sup> Bias bis zu  $\Delta m_t^{\text{MC}} \sim 1 \text{ GeV}$ . Eine realistischere Studie wird eingeführt wo Particle-  
<sup>73</sup> Level-Vorhersagen auf Detector-Level gefalten werden.

<sup>74</sup> Dagegen wirken Top-Quark-Effekte auch im Higgs-Sektor. Anhand des Beispiels  
<sup>75</sup> von Higgs-Paar-Produktion ( $hh$ ) beim LHC wird gezeigt, dass die  $m_t$ -Abhängigkeit  
<sup>76</sup> von  $hh$ -Produktion auf NLO Unterschiede in differentiellen Verteilungen aufweisen  
<sup>77</sup> im Vergleich zu Vorhersagen, wo die Top-Quark-Freiheitsgraden ausintegriert werden.  
<sup>78</sup> Ein vollständiges MC-Package zur Erzeugung von Higgs-Paar-Events (wo die trilineare  
<sup>79</sup> Higgs-Selbstkopplung sowie die Higgs-Top-Yukawakopplung variiert werden können) wird  
<sup>80</sup> präsentiert.



# 81 **Contents**

82	<b>Abstract</b>	v
83	<b>Zusammenfassung</b>	vii
84	<b>Contents</b>	ix
85	<b>1 Introduction</b>	1
86	<b>2 The Standard Model</b>	5
87	2.1 Matter content and gauge interactions . . . . .	5
88	2.2 The Higgs mechanism . . . . .	7
89	2.3 Top-Higgs interactions . . . . .	10
90	2.4 Outstanding issues with the SM . . . . .	11
91	<b>3 Higher-order calculations in hadron-hadron collisions</b>	15
92	3.1 Divergences in QFT . . . . .	15
93	3.1.1 Regularization . . . . .	15
94	3.1.2 Renormalization . . . . .	18
95	3.1.3 Perturbative expansion of QCD . . . . .	18
96	3.2 Infrared divergences . . . . .	20
97	3.3 The factorization theorem . . . . .	21
98	<b>4 Monte-Carlo event generators</b>	25
99	4.1 Matrix-element providers . . . . .	27
100	4.1.1 GoSAM: computation of one-loop amplitudes . . . . .	27
101	4.1.2 Infrared divergence cancellation . . . . .	29
102	4.2 Parton-shower models . . . . .	31
103	4.2.1 Altarelli-Parisi splitting functions . . . . .	31
104	4.2.2 The Sudakov form factor . . . . .	32
105	4.2.3 Parton-shower matching . . . . .	32
106	4.3 Hadronization . . . . .	33
107	4.3.1 Lund string model . . . . .	34
108	4.3.2 Cluster model . . . . .	34
109	<b>5 The LHC and the ATLAS detector</b>	37
110	5.1 The Large Hadron Collider . . . . .	37

## Contents

111	5.2 The ATLAS detector . . . . .	38
112	5.2.1 The Inner Detector . . . . .	39
113	5.2.2 The Liquid Argon (LAr) Calorimeter . . . . .	41
114	5.2.3 The Tile Calorimeter (TileCal) . . . . .	42
115	5.2.4 The Muon Spectrometer . . . . .	42
116	5.2.5 Trigger & Data acquisition . . . . .	42
117	<b>6 Theoretical predictions for <math>t\bar{t}</math> final-states</b>	<b>45</b>
118	6.1 The narrow-width approximation . . . . .	46
119	6.2 $W^+W^-b\bar{b}$ production at NLO QCD . . . . .	48
120	6.3 Calculation setup . . . . .	49
121	6.4 Event requirements . . . . .	51
122	6.5 Total cross-section results . . . . .	51
123	<b>7 NWA versus <math>WWbb</math>: Top-quark mass uncertainties at parton-level</b>	<b>53</b>
124	7.1 The template fit method . . . . .	53
125	7.2 Definition of the observables . . . . .	54
126	7.3 Comparison of the different theoretical descriptions . . . . .	55
127	<b>8 Experimental resolution and bin migration</b>	<b>67</b>
128	8.1 Inverse problems . . . . .	67
129	8.2 Folding setup in ATLAS . . . . .	68
130	8.3 Theoretical descriptions and MC samples . . . . .	69
131	<b>9 Determination of the top-quark mass at detector-level</b>	<b>71</b>
132	9.1 The AnalysisTop setup . . . . .	71
133	9.2 Differential results at particle- and detector-level . . . . .	72
134	9.3 Statistical and systematic cross-checks . . . . .	73
135	9.4 Folded results and template parametrization . . . . .	74
136	9.5 Numerical result for top-quark mass uncertainties . . . . .	75
137	<b>10 Top-mass dependence in Higgs pair production at NLO</b>	<b>77</b>
138	10.1 Theoretical descriptions of $hh$ production . . . . .	77
139	10.1.1 Approximations in the heavy-top limit ( $m_t \rightarrow \infty$ ) . . . . .	77
140	10.1.2 Full NLO QCD prediction in the SM . . . . .	78
141	10.2 The Electroweak Chiral Lagrangian . . . . .	79
142	10.3 Cross-sections for BSM benchmark points . . . . .	80
143	<b>11 Variations of the triple Higgs-coupling and parton-shower effects</b>	<b>83</b>
144	11.1 The POWHEG-BOX framework . . . . .	83
145	11.2 Interfacing two-loop contributions . . . . .	84
146	11.3 Total and differential cross-sections at fixed-order . . . . .	85
147	11.4 Parton-shower matched predictions at NLO . . . . .	86
148	<b>12 Conclusion &amp; Outlook</b>	<b>89</b>

149	<b>Bibliography</b>	<b>91</b>
150	<b>A Studies for <math>t\bar{t}</math> modeling in Herwig 7.1</b>	<b>101</b>



# <sup>151</sup> 1 Introduction

<sup>152</sup> The Standard Model (SM) of Particle Physics is one of the most successful physical  
<sup>153</sup> theories to date. While it still begs some unanswered questions that are outlined below,  
<sup>154</sup> the precision to which its predictions were tested by high-energy colliders, but also in  
<sup>155</sup> low-energy experiments, large-scale universe phenomena, neutrino and other experiments  
<sup>156</sup> is extremely convincing. In particular, it bases on mathematical concepts that allow  
<sup>157</sup> for a significant predictive power. Considering that physicists tend to like a theory  
<sup>158</sup> that contains the least amount of free parameters and a maximal amount of derivable  
<sup>159</sup> parameters, the SM fares rather well: it contains only 19 parameters, namely the angles  
<sup>160</sup> of the Cabibbo-Kobayashi-Maskawa mixing matrix and its CP-violating phase (3 + 1),  
<sup>161</sup> the gauge couplings corresponding to the model's underlying symmetries (3), the lepton  
<sup>162</sup> and quark masses (9), the QCD vacuum angle (1), and the Higgs mass and vacuum  
<sup>163</sup> expectation value (2). Since most of these parameters have been measured to an excellent  
<sup>164</sup> precision, efforts have largely concentrated on the less well-measured parameters, one of  
<sup>165</sup> these being the top-quark mass.

<sup>166</sup> Because the top-quark is the heaviest known elementary particle, with a mass mea-  
<sup>167</sup> sured at  $m_t = 173.0 \pm 0.4$  GeV [1], physicists had to wait until 1995 for its discovery by  
<sup>168</sup> the CDF [2] and DØ [3] experiments at Fermilab, 23 years after it was predicted. Only  
<sup>169</sup> then did the last missing piece of the three quark generations fall into place. Nowadays,  
<sup>170</sup> abundant production of top-quarks with the Large Hadron Collider (LHC) at CERN  
<sup>171</sup> allows for a variety of accurate measurements of its properties. Of particular inter-  
<sup>172</sup> est, the precise determination of its mass is a key to a deeper understanding of modern  
<sup>173</sup> quantum-field theory (QFT). Most notably, the top-quark mass enters global electroweak  
<sup>174</sup> fits which are important for consistency testing of the SM; it also strongly affects correc-  
<sup>175</sup> tions to the Higgs quartic coupling, thus having a large impact on the stability of the  
<sup>176</sup> SM vacuum. Finally, being the only quark with a lifetime surpassing the hadronisation  
<sup>177</sup> scale, it is the only *bare* colored particle produced in SM processes. In general, one has  
<sup>178</sup> to choose an appropriate mass definition, be it a QFT-consistent definition like the pole  
<sup>179</sup> mass (on-shell renormalized) and the  $\overline{\text{MS}}$  mass (renormalized after the short-distance  
<sup>180</sup>  $\overline{\text{MS}}$  scheme), or the less understood Monte-Carlo (MC) mass.

<sup>181</sup> Recently, the ATLAS and CMS experiments, using innovative approaches and analy-  
<sup>182</sup> sis techniques, have been able to reduce the uncertainty of the measured MC top-quark  
<sup>183</sup> mass to about 0.5 GeV. Achieving a more precise determination of the top-quark mass  
<sup>184</sup> constitutes a significant challenge for both sides of the physics community. While on the  
<sup>185</sup> one hand, experimentalists have to find new ideas to drive down the mostly systematics-  
<sup>186</sup> dominated uncertainties, theorists need to improve precision calculations by going to  
<sup>187</sup> higher-order predictions and beyond formerly accepted approximations. The compu-  
<sup>188</sup> tation of higher-order corrections for on-shell top-quark pair ( $t\bar{t}$ ) production has been

## 1 Introduction

189 a major success during the LHC era. The production of a pair of on-shell top-quarks  
190 is referred to as the narrow-width approximation (NWA). Because the corrections to  
191 NWA calculations are expected to be small, of order  $\mathcal{O}(\Gamma_t/m_t) < 1\%$  for inclusive cross-  
192 sections, most fixed-order predictions aim at computing higher-order QCD and EW  
193 corrections to top-quark pair production in this approximation.

194 The experimentalists, though, reconstruct the top-quark pair from their decay prod-  
195 ucts, i.e. from the dilepton, lepton+jets or all-hadronic final-states, depending on the  
196 decay channel of the top and antitop-quarks. Instead, the fixed-order prediction of a  
197 fully-decayed  $t\bar{t}$  final-state is computationally demanding: instead of a  $2 \rightarrow 2$  process,  
198 the final-state phase space becomes that of a  $2 \rightarrow 4$  (for  $pp \rightarrow W^+W^-b\bar{b}$ ) or a  $2 \rightarrow 8$   
199 process (including  $W$ -boson decays). A computation of the full final-state prediction at  
200 next-to-leading order (NLO) comprises Feynman diagrams that are not present in the  
201 NWA: some do not contain double-resonant top-quarks, and others include internal lines  
202 between the top-quark decay legs, i.e. the latter do not factorize. In fact, the additional  
203 interference terms can be of importance to distributions that are sensitive to higher-order  
204 and off-shell effects, for example in phase-space regions populated first at higher-order in  
205 QCD. In this work, we first briefly present the foundations of the SM including the Higgs  
206 mechanism and the relation between the Higgs sector and the top-quark in Chapter 2.  
207 In Chapter 3, the basics of higher-order calculations are summarized: the appearance  
208 of UV and IR divergences in loop corrections and the way to deal with them (regulari-  
209 zation and renormalization), the perturbative expansion for QCD at high energies from  
210 the running of the strong coupling  $\alpha_s$ , and the factorization theorem for hadron-hadron  
211 collisions are laid out in some detail. Finally, we concentrate on MC event genera-  
212 tors in Chapter 4 and explain the ingredients needed for particle-level event generation.  
213 Switching to the experimental side, the LHC and in particular the ATLAS detector are  
214 presented in Chapter 5. At that point, the different theoretical descriptions of top-quark  
215 pair production are discussed in Chapter 6. With the example of top-quark pair pre-  
216 dictions in the  $e\mu$  dilepton channel, we show how higher-order and off-shell effects can  
217 have a sizeable impact on an experimental MC top-quark mass extraction in Chapter 7.  
218 There, four different theoretical descriptions are compared with respect to an experimen-  
219 tally realistic top-quark mass extraction for  $pp \rightarrow W^+(\rightarrow \ell^+\nu_\ell)W^-(\rightarrow \ell^-\bar{\nu}_\ell)b\bar{b}$ . In the  
220 NWA, we produce top-quark pairs at NLO QCD, and describe the top-decay at different  
221 accuracies: LO, respectively NLO QCD, as well as operated by a parton-shower. We  
222 compare the NWA results to a full  $W^+W^-b\bar{b}$  computation at NLO QCD. Taking into  
223 account detector reconstruction efficiencies and bin migration effects, which is the sub-  
224 ject of Chapter 8, we then quantify the shift in the extracted top-quark mass in an exact  
225 ATLAS framework in Chapter 9, where distributions are folded up to detector-level.

226 Looking at another sector entirely, we emphasize that top-quarks also play an im-  
227 portant role in calculations for the production of one or several Higgs bosons at the  
228 LHC. Because the top-quark is the heaviest SM particle and since the Higgs boson's  
229 coupling to fermions is proportional to their mass, higher-order corrections to Higgs  
230 processes mainly happen through top-quark loops. For instance, single Higgs produc-  
231 tion at the LHC is dominated by gluon-fusion with a top-quark loop intermediate state  
232 (loop-induced production), i.e. higher-order corrections to  $gg \rightarrow h$  start at two-loop

level already. The same holds for the production of a pair of Higgs bosons: this is of particular interest, since di-Higgs production is the main channel for probing the trilinear Higgs self-coupling. The best limit set on the Higgs self-coupling's ratio  $\kappa_\lambda$  to the SM predicted value is given by ATLAS at  $-5.0 \leq \kappa_\lambda \leq 12.1$  [4]. We show, within a non-linear Effective Field Theory (EFT) framework allowing to vary the Higgs couplings, that the full  $m_t$ -dependence of di-Higgs production at NLO QCD has important effects, especially on differential cross-section predictions. In Chapter 10, the electroweak chiral Lagrangian (EWChL), which is a non-linear realization of an EFT, is introduced. The results for NLO di-Higgs cross-sections and differential distributions with variations of the Higgs couplings are presented at 13 TeV for BSM benchmark points. Finally, the implementation of the full  $m_t$ -dependent NLO corrections for di-Higgs production into the POWHEG-BOX-V2 event generator is the subject of Chapter 11. In this package, variations of the trilinear Higgs self-coupling and the top-Higgs Yukawa coupling are possible. We show studies comparing differential distributions for fixed-order NLO to parton-shower matched predictions, and discuss parton-shower related uncertainties. Finally, we summarize the current state of the SM and outline future, potentially interesting developments in both top-quark and Higgs physics.



## 250 2 The Standard Model

251 The SM was developed and supplemented over five decades, and describes all elementary  
252 particles and their interactions via three of the four fundamental forces in a quantum-field  
253 theoretical framework: the electromagnetic, weak and strong interactions. Although it  
254 is known that the SM suffers from some theoretical shortfalls that were described briefly  
255 in Chapter 1, there is, to date, no experimental evidence that directly contradicts it.

256 At the core, the discovery by Glashow, Salam and Weinberg [5, 6, 7] that the elec-  
257 tromagnetic and weak interactions could be embedded in a unified theory constitutes  
258 the first stone of the SM edifice. What if all known forces and particles could be de-  
259 scribed by the same, unique theory? Since that time, the electroweak (EW) theory of  
260 interactions gradually incorporated the quantum chromodynamics (QCD) sector, which  
261 describes the strong interaction. The addition of the Higgs mechanism, that generates  
262 mass terms for the fermions and gauge bosons, culminated in what is known today as the  
263 SM Lagrangian. The SM is one of the most successful theories up-to-date, and has been  
264 extensively tested against experimental data. A comprehensive comparison of computed  
265 cross-sections for SM processes to values measured by ATLAS, shown in Fig. 2.1, makes  
266 for a compelling argument in favour of the SM’s predictive power.

### 267 2.1 Matter content and gauge interactions

268 The SM is a quantum-field gauge theory: the known elementary particles are interpreted  
269 as the excitations of quantized fields, and their interactions are described by the exchange  
270 of gauge bosons. Both matter- and gauge fields obey certain rules under the correspond-  
271 ing gauge transformations: that is, they transform according to different representations  
272 of the underlying gauge group. The SM builds on the

$$SU(3)_C \times SU(2)_L \times U(1)_Y$$

273 gauge group. It is the product group of the QCD group  $SU(3)_C$ , and its corresponding  
274 color quantum number  $C$ , and the electroweak group  $SU(2)_L \times U(1)_Y$ , that distinguishes  
275 left- from right-handed particles as doublets, respectively singlets under the group trans-  
276 formation, and the  $U(1)_Y$  group’s quantum number is the so-called hypercharge  $Y$ . The  
277 fermionic matter fields are classified into left-handed leptons and quarks, both transform-  
278 ing as doublets under the  $SU(2)_L$  group, and their singlet right-handed counterparts.  
279 There are furthermore three distinct copies, called generations, or families:

## 2 The Standard Model

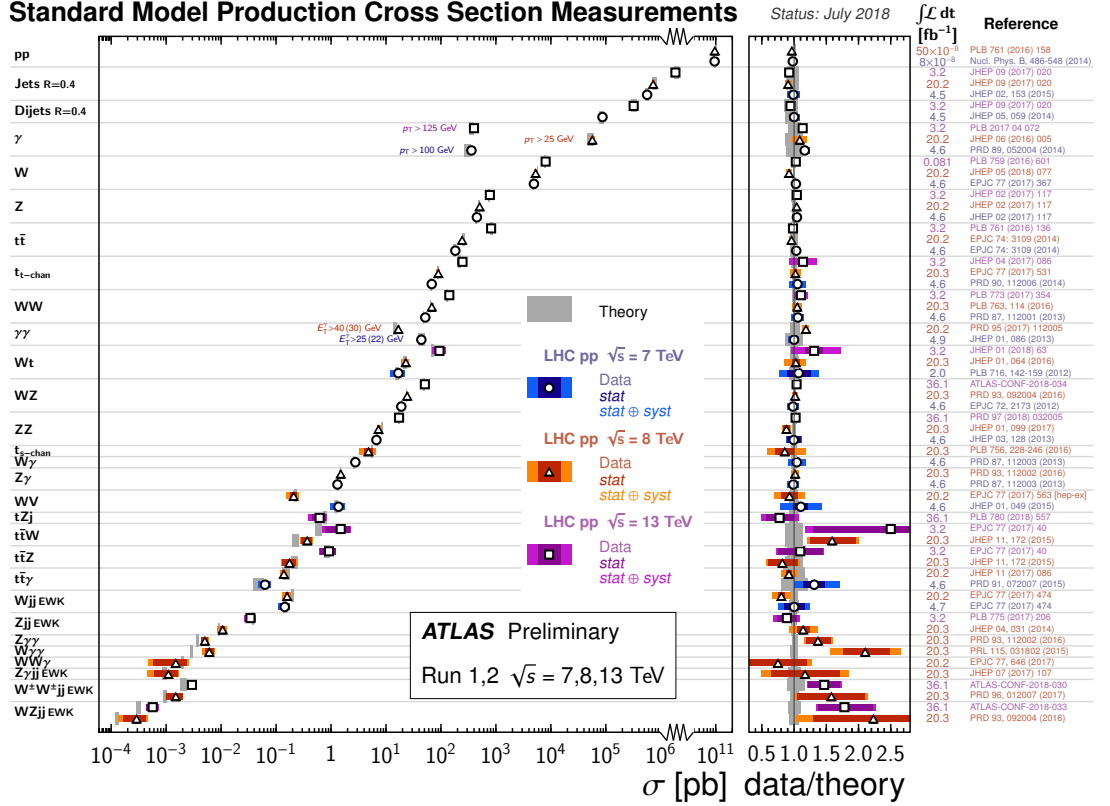


**Figure 2.1:** The predicted cross-sections (in gray, where bands represent the theoretical uncertainty) for SM production processes at LHC center-of-mass energies of  $\sqrt{s} = 7, 8, 13$  TeV are compared to their measured values at the ATLAS experiment (in color). On the right, the ratio of data to theory is shown to be compatible with 1.

$$\begin{pmatrix} \nu_e \\ e^- \end{pmatrix}_L, \quad \begin{pmatrix} u \\ d' \end{pmatrix}_L \quad \begin{pmatrix} \nu_\mu \\ \mu^- \end{pmatrix}_L, \quad \begin{pmatrix} c \\ s' \end{pmatrix}_L \quad \begin{pmatrix} \nu_\tau \\ \tau^- \end{pmatrix}_L, \quad \begin{pmatrix} t \\ b' \end{pmatrix}_L$$

$$e_R^-, \quad u_R, \quad d'_R \quad \mu_R^-, \quad c_R, \quad s'_R \quad \tau_R^-, \quad t_R, \quad b'_R$$

and their corresponding antiparticles. The quark weak eigenstates mix via the unitary Cabibbo-Kobayashi-Maskawa (CKM) matrix to give the physical mass eigenstates:

$$\begin{pmatrix} d' \\ s' \\ b' \end{pmatrix} = \begin{pmatrix} V_{ud} & V_{us} & V_{ub} \\ V_{cd} & V_{cs} & V_{cb} \\ V_{td} & V_{ts} & V_{tb} \end{pmatrix} \begin{pmatrix} d \\ s \\ b \end{pmatrix}.$$

The quarks are the only matter fields carrying color charge, and live in the triplet (**3**), respectively anti-triplet (**3̄**) representations of the  $SU(3)_C$  group. The color quantum numbers are defined as red, blue and green, respectively anti-red, anti-blue and anti-green. That is, for the up- and down-quark:

$$\begin{pmatrix} u_r \\ u_b \\ u_g \end{pmatrix}, \quad \begin{pmatrix} d_{\bar{r}} \\ d_{\bar{b}} \\ d_{\bar{g}} \end{pmatrix} \in SU(3)_C.$$

286 Governing the interactions, the gauge bosons corresponding to each subgroup couple  
 287 with a separate strength to the matter fields:

- 288 • three  $W_\mu^a$ ,  $a = (1, 2, 3)$ , bosons belonging to  $SU(2)_L$ , coupling with strength  $\propto g$
- 289 • one  $B_\mu$  boson belonging to  $U(1)_Y$ , coupling with strength  $\propto g'$
- 290 • eight gluon fields  $G_\mu^a$ ,  $a = (1, \dots, 8)$ , belonging to  $SU(3)_C$ , with coupling  $\propto g_s$

291 By the principle of gauge covariance, the interaction terms between gauge bosons and  
 292 the rest of the particle fields are given by promoting the 4-derivatives in the kinetic terms  
 293 of the corresponding sector to covariant derivatives:

$$\partial_\mu \rightarrow D_\mu = \left[ \partial_\mu + ig \frac{\sigma_a}{2} W_\mu^a + ig' \frac{Y}{2} B_\mu \right] \quad (\text{EW}) \quad (2.1)$$

294

$$\partial_\mu \rightarrow D_\mu = [\partial_\mu + ig_s T_a G_\mu^a] \quad (\text{QCD}) \quad (2.2)$$

295 where  $\sigma_a$  are the three Pauli matrices (the generators of the Lie algebra of  $SU(2)_L$ ),  
 296 and  $T_a$  are the eight generators of the Lie algebra of  $SU(3)_C$ . The replacement by a  
 297 covariant derivative also induce gauge boson self-coupling interactions

298 Finally, analogously to the quarks, the electroweak gauge bosons mix to give rise to  
 299 the physical charged– and neutral-current interaction bosons:

$$W^\pm = \frac{1}{\sqrt{2}} (W^1 \mp iW^2) \quad (2.3)$$

$$\begin{pmatrix} \gamma \\ Z \end{pmatrix} = \begin{pmatrix} \cos(\theta_W) & \sin(\theta_W) \\ -\sin(\theta_W) & \cos(\theta_W) \end{pmatrix} \begin{pmatrix} B \\ W^3 \end{pmatrix} \quad (2.4)$$

300 where  $\theta_W$  is the Weinberg angle.

## 301 2.2 The Higgs mechanism

302 If one writes down the most general, renormalizable Lagrangian for the model above,  
 303 two problems appear:

- 304 • the usual Dirac mass terms appearing in the fermionic sector are not invariant  
 305 under  $SU(2)_L$
- 306 • mass terms for the  $W^\pm$ ,  $Z$  bosons are not gauge-invariant

## 2 The Standard Model

307 So, in order to generate masses for the aforementioned particles, an external con-  
 308 traption is needed. The Brout-Englert-Higgs [8, 9, 10] mechanism proposed in 1964  
 309 introduces a new spin-0 fundamental  $SU(2)_L$  doublet, called the Higgs field:

$$\phi(x) = \begin{pmatrix} \phi^+(x) \\ \phi^0(x) \end{pmatrix} \quad (2.5)$$

310 It is colorless, and is charged under the electroweak  $U(1)_Y$  symmetry. The  $SU(3)_C \times$   
 311  $SU(2)_L \times U(1)_Y$  Lagrangian gets completed by a (gauged) Higgs sector, where the  
 312 covariant derivative  $D_\mu$  is given by Eq. (2.1):

$$\mathcal{L}_h = (D_\mu \phi)^\dagger (D^\mu \phi) + V(\phi) \quad (2.6)$$

$$= (D_\mu \phi)^\dagger (D^\mu \phi) + \mu^2 \phi^\dagger \phi - \lambda (\phi^\dagger \phi)^2, \quad \lambda > 0 \quad (2.7)$$

313 Similarly to the case of superconductivity, the underlying  $SU(2)_L \times U(1)_Y$  symme-  
 314 try can be spontaneously broken if the Higgs potential  $V(\phi)$  has a non-zero ground  
 315 state. This is the case for the *Mexican-hat* potential given above, which is pictured in  
 316 Fig. 2.2. When the Higgs field assumes one of the degenerate ground states with a vac-  
 317 uum expectation value at the minimum of the potential around  $v = \mu/\sqrt{\lambda} \sim 246$  GeV,  
 318 it spontaneously breaks the  $SU(2)_L \times U(1)_Y$  symmetry of the Lagrangian.

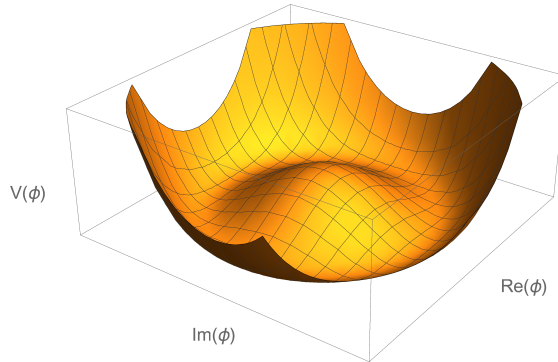


**Figure 2.2:** The  $SU(2) \times U(1)$  symmetric Higgs Mexican-hat potential has a degenerate non-zero ground state at  $v^2 = \langle \phi_0^\dagger \phi_0 \rangle \sim (246 \text{ GeV})^2$ .

319 Expanding the Higgs field from Eq. (2.5) around the vacuum and taking the EW  
 320 covariant derivative from Eq. (2.1),

$$\phi(x) = \frac{1}{\sqrt{2}} \begin{pmatrix} 0 \\ v + h(x) \end{pmatrix} \quad (2.8)$$

$$D_\mu \phi(x) = \frac{1}{\sqrt{2}} \left( \partial_\mu h(x) - \frac{i}{2} \left( W_\mu^1 - iW_\mu^2 \right) (v + h(x)) - \frac{i}{2} \left( g'B_\mu - gW_\mu^3 \right) (v + h(x)) \right), \quad (2.9)$$

## 2.2 The Higgs mechanism

the Higgs field naturally couples to the gauge bosons. Finally, computing the squared gauged kinematic term of the spontaneously broken Higgs field from Eq. (2.7), and replacing the gauge fields with their physical rotated states from Eqs. (2.3), (2.4) gives:

$$\begin{aligned} \mathcal{L} \supset & \frac{1}{2}(\partial_\mu h)(\partial^\mu h) + \frac{g^2 v^2}{4} W_\mu^+ W^{-\mu} + \frac{1}{2} \left( \frac{(g^2 + g'^2)v^2}{4} \right) Z_\mu Z^\mu \\ & + \frac{1}{2}(2\lambda v^2 h^2) + \lambda v h^3 + \frac{\lambda}{8} h^4 \end{aligned} \quad (2.10)$$

So, the dynamic EW spontaneous breaking (EWSB) of the Higgs potential generates masses for the  $W^\pm$ ,  $Z$  gauge bosons and identifying the mass terms in the Lagrangian leads to following leading-order boson mass relations<sup>1</sup>:

$$\begin{aligned} m_H &= \sqrt{2\lambda}v \\ m_W &= \frac{gv}{2} & \cos(\theta_W) &= \frac{g}{\sqrt{g^2 + g'^2}} \\ m_Z &= \frac{\sqrt{g^2 + g'^2}v}{2} & \sin(\theta_W) &= \frac{g'}{\sqrt{g^2 + g'^2}} \\ m_\gamma &= 0 \end{aligned}$$

328 The  $W$  and  $Z$  boson masses are related (at tree-level):

$$m_W = m_Z \cos(\theta_W).$$

with the experimentally measured values  $m_W = 80.385$  GeV,  $m_Z = 91.1876$  GeV and the Weinberg angle  $\theta_W = 0.2223$ . Finally, considering the last two terms in Eq. (2.10), the Higgs couples to itself to produce the Feynman diagrams shown in Fig. 2.3.

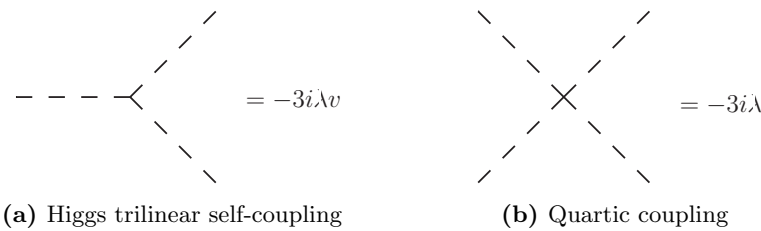


**Figure 2.3:** The physical Higgs field couples to itself after EWSB. The Feynman rules are given for (a) the triple vertex and (b) the quartic vertex.

<sup>1</sup>The covariant terms in the Dirac propagator also give rise to the quark masses,  $\mathcal{L} \supset \frac{m_f}{2v} \bar{\psi}_f \psi h$

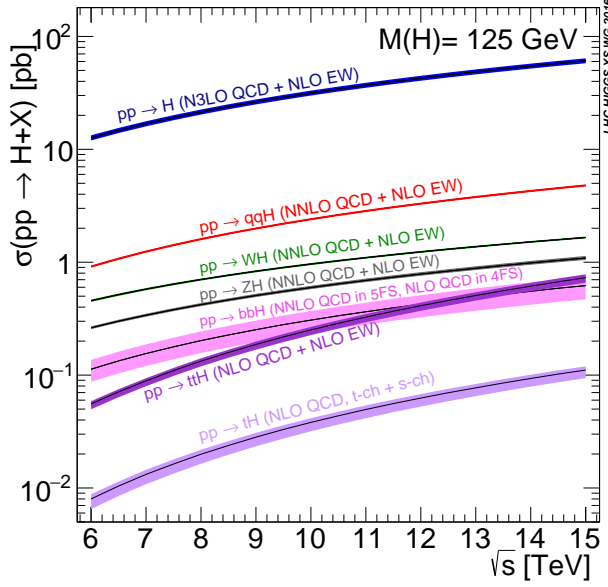


**Figure 2.4:** Theory prediction for  $pp \rightarrow h + X$  production cross-sections as a function of the center-of-mass energy  $\sqrt{s}$ . Single Higgs production at the LHC is dominated by gluon fusion mediated by a top-quark loop.

### 332 2.3 Top-Higgs interactions

333 Intrinsically, the top-quark is tightly linked to the Higgs boson properties and has gen-  
 334 erally strong phenomenological implications for the Higgs sector. Because it is the  
 335 heaviest SM elementary particle, and since the Yukawa coupling of the Higgs boson  
 336 to fermions is proportional to their masses, the Higgs couples strongest to the top-quark  
 337 (in comparison, bottom-quark effects in inclusive Higgs observables are of the order of  
 338  $m_b/m_t = 2.8\%$ ). It is especially important for Higgs production at the LHC: the pre-  
 339 dominant production mechanism happens by gluon-fusion via a triangle top-quark loop,  
 340 as shown in Fig. 2.4. In comparison, other associated production modes have cross-  
 341 sections that are more than one order of magnitude smaller. The Feynman diagrams for  
 342 the main production channels observed at LHC are also depicted in Fig. 2.5.

343 In relation to both the measurement of the Higgs triple self-coupling and the impor-  
 344 tance of top-mass effects in Higgs production, the reader is referred to the extensive  
 345 discussion laid out in Chapter 10. Not only do top-quarks influence Higgs processes  
 346 cross-sections at collider experiments, but they also have a deeper connection to the  
 347 Higgs potential. Indeed, the RGE  $\beta$ -function of the Higgs quartic coupling (which gov-  
 348 erns the evolution of the coupling's value at different resolution scales, see Chapter 3)  
 349 is sensitive to renormalization counterterms stemming from top-quark loops. Eq. (2.11)  
 350 gives the one-loop  $\beta$ -function for the Higgs quartic coupling [11]:

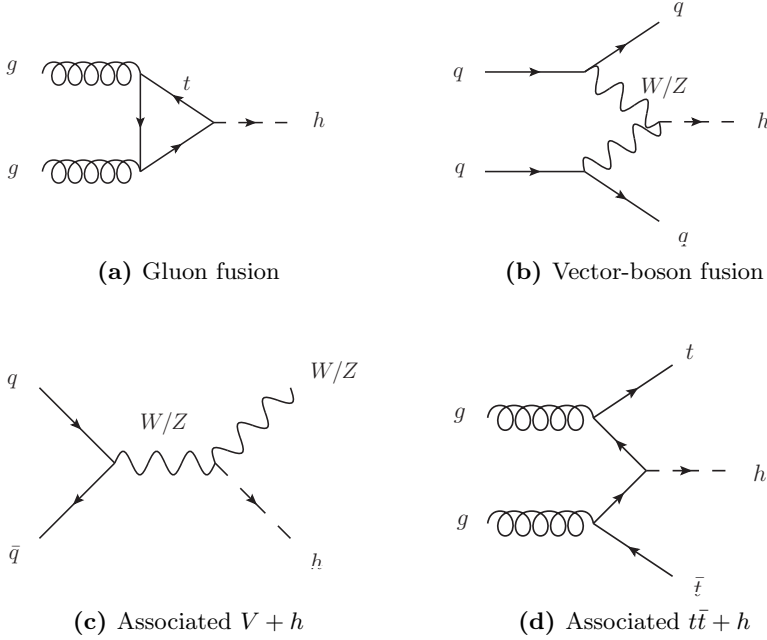


**Figure 2.5:** Leading-order diagrams for Higgs production by (a) gluon fusion, (b) vector-boson fusion, (c) associated vector production and (d) associated  $t\bar{t}$  production.

$$\mu^2 \frac{d\lambda}{d\mu^2} = \beta_\lambda(\lambda, y_t, g_s, \dots) = \frac{1}{16\pi^2} (12\lambda^2 + 6\lambda y_t^2 - 3y_t^4), \quad y_t = \sqrt{2} \frac{m_t}{v} \sim 1 \quad (2.11)$$

where  $y_t$  is the top-Yukawa coupling and is proportional to the top-quark mass  $m_t$ . Because the top-Yukawa coupling is non-negligible, small variations in the value of the top-quark mass modify the evolution of the Higgs quartic coupling  $\lambda$  in a untrivial way. If  $\lambda(\mu)$  was to become negative at scales much below the Planck scale,  $M_P \sim 10^{18} - 10^{19}$  GeV (see Fig. 2.6a), the Higgs field could tunnel from the current false vacuum state to the true, absolutely stable vacuum ground state. Current measurements seem to support the fact that the SM is in a metastable state, as shown in Fig. 2.6b. For the existentially anxious reader, a state-of-the art calculation of the EW vacuum decay rate can be found in Ref. [12].

## 2.4 Outstanding issues with the SM

For all its successes, the SM is known to have some theoretical flaws. Below is a list of familiar shortcomings:

- **Massless neutrinos:** In the SM, neutrinos are naturally massless. Experiments [15] have shown that neutrinos can oscillate between the different families,

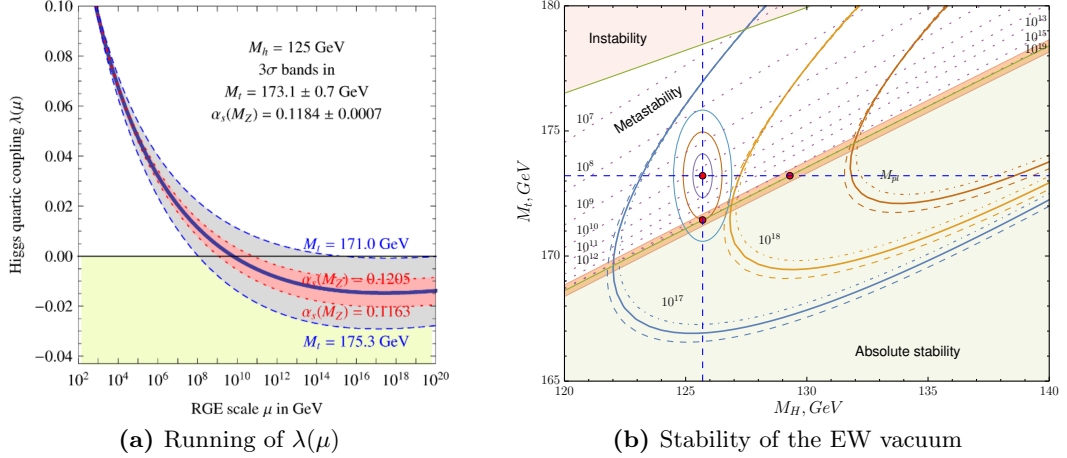


**Figure 2.6:** (a) The RGE evolution of the Higgs quartic coupling  $\lambda$  can lead to negative values at high energy scales (around the Planck scale  $\sim M_P$ ). This in turn makes the EW vacuum potentially unstable. The running is highly dependent on the top-quark mass and  $\alpha_s$  values [13]. (b) The SM point, in red, is plotted in the  $(m_h, m_t)$  phase-space with  $1-, 2-$  and  $3\sigma$  uncertainties. The pink dotted lines indicate contours where  $\lambda(\mu) = 0$  for the indicated values of  $\mu$ , and the parabolic curves where the beta-function  $\beta_\lambda(\mu) = 0$  for chosen values of  $\mu$ . The measured Higgs and top-quark masses point to a SM universe close to the metastable region [14].

and this requires a mixing of flavour states with mass eigenstates, similarly to the CKM mixing. Different mechanisms were introduced to generate neutrino masses: a right-handed (so-called *sterile*) neutrino could exist, and not interact with matter (no right-handed neutrino was ever observed), or neutrinos could acquire a Majorana mass. Some R-parity violating supersymmetric (SUSY) models also produce neutrino masses.

- **Gravity:** General relativity is believed to be incompatible with the SM under its current form, and a unified theory of all four interactions is still missing. An exchange gravitational gauge-boson can be introduced under the form of a spin-2 particle, called the graviton. The addition of corresponding terms to the SM Lagrangian introduces UV divergences that cannot be handled by a finite number of counterterms, though, and the theory is not perturbatively renormalizable.
- **Dark matter:** The presence of dark matter in the Universe has been proved from multiple cosmological observations. Yet, the SM does not contain a good dark matter candidate particle. Some extensions, in particular SUSY, provide a heavy non-decaying particle (the lightest in the SUSY spectrum, called light supersymmetric particle (LSP)) that turns out to be a good candidate.

## 2.4 Outstanding issues with the SM

- **Baryon asymmetry:** The SM assumes that matter and antimatter should have been produced almost symmetrically at the Big Bang. Yet baryons are observed to be in overwhelming excess over antibaryons.
- **Hierarchy problem:** There is a manifest unbalance between the three unified forces of the SM and gravity, or between their respective mass scales. In particular, it is not clear why the Higgs boson mass is so small with respect to the Planck scale: basically, radiative corrections to the Higgs self-energy should blow up its mass, and the observed value of  $m_h = 125$  GeV requires an incredible amount of fine-tuning to cancel the radiative corrections. Again, SUSY models solve this problem by requiring every SM particle to have a supersymmetric partner which has the opposite spin-statistics: their contributions to the Higgs mass then cancel naturally.

Although all model extensions of the SM have respective advantages over the current theory, none of the particles predicted by them has been observed at the LHC or any other experiment yet.



397 **3 Higher-order calculations in  
hadron-hadron collisions**

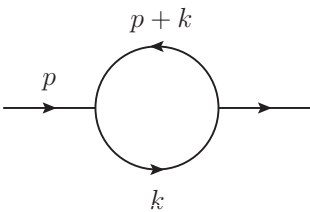
398

399 The SM Lagrangian presented in the last Chapter provides the corresponding Feynman  
400 rules with which to compute theoretical cross-sections. As will be explained in Sec-  
401 tion 3.1.3, the scattering amplitudes can be calculated perturbatively, introducing one  
402 loop per additional higher order in the perturbative series. Since the first successes of  
403 QFT in predicting basic energy spectrum properties and leading-order (LO) scattering  
404 amplitudes, there has always been a need for a more consistent framework in which  
405 higher-order corrections could be worked out. In this Chapter, we summarize the im-  
406 portant ingredients used in most theoretical computations nowadays, in particular in the  
407 context of high-energy hadron-hadron collisions.

408 **3.1 Divergences in QFT**

409 Going beyond LO in the computation of scattering matrix-elements, one encounters two  
410 classes of divergences. Consider a one-loop scalar massless two-point function, where  
411 the internal loop-momentum is integrated over:

412



$$I_2(p^2; 0, 0) = \int_{-\infty}^{\infty} \frac{d^4 k}{(2\pi)^4} \frac{1}{(k^2 + i\delta)((p+k)^2 + i\delta)}. \quad (3.1)$$

413 In the limit  $|k| \rightarrow \infty$ , the integral behaves as  $I \propto \int \frac{dk k^3}{k^2 \cdot k^2} = \int \frac{dk}{k}$  which is logarithmi-  
414 cally divergent. The integral is also divergent when taking the limit  $k \rightarrow 0$ . These are  
415 called *ultraviolet*, respectively *infrared* divergences.

416 As a solution to the infinities conundrum, the above integral has to be treated by the  
417 introduction of a UV cutoff of some kind – this is a method called *regularization*, and  
418 by absorbing the regularized infinities in a consistent way through the *renormalization*  
419 of the Lagrangian bare couplings and masses.

420 **3.1.1 Regularization**

421 A first attempt at controlling UV divergences consists in the introduction of a high-  
422 momentum regulator  $k^2 < \Lambda^2$ . Then, the loop integral given in Eq. (3.1) behaves as

$$I_2(p^2; 0, 0) \propto \int_{\epsilon}^{\Lambda} \frac{dk}{k} \sim \log(\Lambda), \quad (3.2)$$

and the integral diverges logarithmically in the cutoff  $\Lambda$ . This is typical of renormalizable theories. Now, obviously, any physical observable should not depend on the value of the arbitrary cutoff, and in practice it does not.<sup>1</sup> As a theoretical downside, the introduction of the cutoff breaks gauge-invariance. It also breaks translational invariance and makes it impossible to use Feynman parameters and the corresponding variable replacements  $p \rightarrow p + k$ .

A possible gauge-invariant regularization method is the so-called Pauli-Villars regularization: a much more massive particle is introduced and its contribution subtracted from the ordinary propagator, that is:

$$\int \frac{d^4 k}{(2\pi)^4} \frac{1}{k^2 + i\delta} \rightarrow \int \frac{d^4 k}{(2\pi)^4} \left( \frac{1}{k^2 + i\delta} - \frac{1}{k^2 - M^2 + i\delta} \right). \quad (3.3)$$

The Pauli-Villars technique cannot be applied to QCD because it is not gauge-covariant, though. On the same stance, it introduces an unphysical field that violates the spin-statistics theorem (it amounts to a spurious scalar field with Fermi statistics). One of the preferred regularization methods nowadays is dimensional regularization. It was refined by 't Hooft and Veltman to regularize any integrals, is gauge-invariant and works for non-Abelian theories as well. The governing idea is that quantum-field theories in a smaller number of dimensions have a lesser superficial degree of divergence. The four dimensions of space-time are therefore analytically continued to  $d = 4 - 2\epsilon$  dimensions, and the integral in Eq. (3.1) can be cast into the following form:

$$I_2(p^2; 0, 0) = \mu^{2\epsilon} \int \frac{d^d k}{(2\pi)^d} \frac{1}{(k^2 + i\delta)((p+k)^2 + i\delta)} \quad (3.4)$$

where the renormalization scale  $\mu$  is a dimensionful parameter needed to keep the integral dimensionless. Then the integral can be worked out by introducing Feynman parameters and Wick-rotating to give the analytical result

$$I_2(p^2; 0, 0) = \frac{1}{\epsilon} + \ln \frac{\mu^2}{-p^2 - i\delta} + 2 + \mathcal{O}(\epsilon) \quad (3.5)$$

where the UV divergences now appear as (at most double, at one-loop) poles in the dimensional regulator  $\epsilon$ . A general dimensionally-regularized one-loop scalar integral with  $n$  external legs has the form:

---

<sup>1</sup>For a fun exercise of trying out different forms of cutoff (Gaussian, Dirac-delta,...), see Ref. [16] for the case of the vacuum polarization in the Casimir effect.

447

$$I = \mu^{n-d/2} \int \frac{d^d k}{(2\pi)^d} \prod_{j=1}^n \frac{1}{(q_j^2 - m_j^2 + i\delta)} \quad (3.6)$$

448 where the internal momenta  $q_j = k + \sum_{i=1}^j p_i$  are expressed as a linear combination of  
 449 the loop momentum  $k$  and the external momenta  $p_i$ . Systematic Feynman parameters  
 450 can be found for the integral above, and generally it can be recast into the form

$$I = \Gamma(n - d/2) \prod_{i=1}^n \int_{0 \leq x_i \leq 1} dx_i \delta \left( 1 - \sum_{j=1}^n x_j \right) \frac{\mathcal{U}^{n-d}(\vec{x})}{\mathcal{F}^{n-d/2}(\vec{x}, p_i \cdot p_j, m_i^2)} \quad (3.7)$$

451 The  $x_1, \dots, x_n$  are the Feynman parameters, and  $\mathcal{U}$ ,  $\mathcal{F}$  are the first, respectively  
 452 second Symanzik polynomials.<sup>2</sup> Then, one needs only perform the integration over  
 453 the Feynman parameters. Most importantly, all one-loop integrals can be reduced to a  
 454 linear combination of a set of *master integrals* that are at most box-diagrams: a one-loop  
 455 master integral basis is thus composed of at most tadpoles, bubbles, triangles and boxes,  
 456 which are all known analytically and implemented in integral libraries. Finally, for tensor  
 457 integrals where the numerator of Eq. (3.6) contains Lorentz indices, there exist methods  
 458 for their reduction to a set of scalar integrals, like the systematic Passarino-Veltman  
 459 method [17] which uses a form factor expansion to factorize the indices. For the interested  
 460 reader, Refs. [18, 19] supply a comprehensive examination of various techniques for  
 461 reducing and evaluating Feynman integrals.

462 Dimensional regularization has lots of benefits, and the algebra is quite straightfor-  
 463 ward. Its major disadvantage is that the Dirac algebra for fermions has to be analytically  
 464 extended to  $d = 4 - 2\epsilon$  spacetime dimensions as well, which is not trivial. The Dirac  
 465 matrices obey an analytically continued Clifford algebra

$$\{\gamma^\mu, \gamma^\nu\} = 2g^{\mu\nu} \quad (3.8)$$

466 with a  $d$ -dimensional metric,  $g^{\mu\nu}g_{\mu\nu} = d$ , where it is but unclear what happens to the  
 467 last Dirac matrix  $\gamma_5 = i\gamma_0\gamma_1\gamma_2\gamma_3$ . The different ways of treating  $\gamma_5$  and the helicities of  
 468 external and internal particle fields lead to different regularization schemes. Note that  
 469 physical observables do not depend on the chosen scheme. In the dimensional reduction  
 470 scheme (DRED) which we use for the predictions given in Chapters 6- 11, the Dirac  
 471 algebra is left to  $d = 4$  dimensions, and the same holds for all external momenta and  
 472 helicities. Only the internal momenta are analytically continued to  $d$ -dimensions.

---

<sup>2</sup>Eq. (3.7) can also be generalized to a Feynman integral for  $l$  loops,  $n$  external and  $m$  internal momenta

### 473 3.1.2 Renormalization

474 As a way to treat the infinities arising from the UV region of integration, the bare param-  
 475 eters of the Lagrangian are redefined to absorb the divergent contributions. Although  
 476 this seems mathematically shaky, it is remarkable that the redefinition of a finite number  
 477 of parameters allows for the treatment of divergences order-by-order and for all Feynman  
 478 diagrams contributing to the amplitude of a renormalizable theory. In practice, renor-  
 479 malization of the Lagrangian is achieved by rewriting the bare masses and couplings  $m_0$   
 480 and  $g_0$  as well as the fields themselves  $\psi_0$ , as a physical (measurable) parameter and a  
 481 counterterm

$$\begin{aligned} m_0 &= Z_m m = m + \delta m \\ g_0 &= Z_g g = g + \delta g \\ \psi_0 &= \sqrt{Z} \psi \end{aligned} \tag{3.9}$$

482 The only requirement is that diagrams corresponding to the counterterms should can-  
 483 cel UV divergences stemming from the bare Lagrangian. In principle, the procedure does  
 484 not define how to handle the finite terms accompanying these diagrams: depending on  
 485 the additional criteria, several renormalization schemes can be chosen (on-shell, MS,  $\overline{\text{MS}}$ ,  
 486 or others). Here as well, the physical observables should be independent of the choice  
 487 of scheme (the top-quark mass is a fringe example and will be discussed summarily in  
 488 Chapter 6).

489 The physical parameters entering the Lagrangian, e.g. the masses and couplings  $m, g$ ,  
 490 have to be determined by experiment. By definition, they are measured at a given energy  
 491 scale. Colloquially, a renormalization starting point is chosen: the couplings/masses are  
 492 then said to *run* with the scale at which they are defined. Notably, the renormalized field  
 493 theory runs according to the Callan-Symanzik equation, which governs the dependence  
 494 of the  $n$ -point correlation functions on the model's parameters by asking that the bare  
 495 Green's functions  $G_0^{(n)}(x_1, \dots, x_n; m_0, g_0)$  do not depend on the changes given in Eq. (3.9):

$$\left( m \frac{\partial}{\partial m} + \beta(g) \frac{\partial}{\partial g} + n\gamma \right) G^{(n)}(x_1, \dots, x_n; m, g) = 0 \tag{3.10}$$

496 where the  $\beta$ -function of the theory is defined as  $\beta(g) = \frac{m}{\delta m} \delta g$ , and the anomalous  
 497 dimension is given by  $\gamma = \frac{m}{\delta m} \frac{\delta \sqrt{Z}}{\sqrt{Z}}$ . Eq. (3.10) is an example of a broad class of evolution  
 498 equations called renormalization group equations (RGE).

### 499 3.1.3 Perturbative expansion of QCD

500 From the running of the strong coupling constant given by the QCD  $\beta$ -function,

$$\mu_R^2 \frac{\partial \alpha_s}{\partial \mu_R^2} = \beta(\alpha_s) = - (b_0 \alpha_s^2 + b_1 \alpha_s^3 + \dots), \tag{3.11}$$

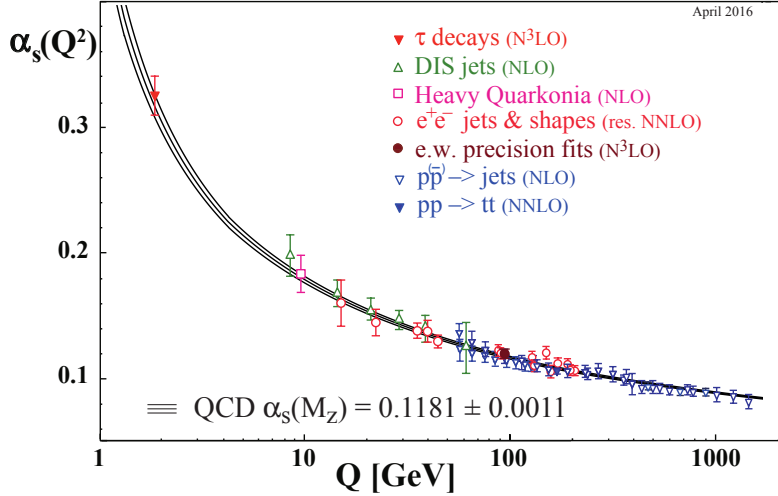


**Figure 3.1:** Various measurements of the strong coupling  $\alpha_s(Q^2)$  at different energy scales  $Q$  show the running behaviour typical of QCD, with a coupling strength that becomes smaller at higher energies, and a Landau pole at the hadronization scale  $Q = \Lambda \sim 1 \text{ GeV}$ .

one sees that because of the negative sign in Eq. (3.11), the strong coupling  $\alpha_s(\mu_R^2)$  becomes smaller at higher scales  $\mu_R^2$ . This running is manifest in Fig. 3.1, which shows measurements of the strong coupling  $\alpha_s$  at different energy scales  $Q$ , in agreement with the QCD theory prediction. Thus, with the measured value of the strong coupling at intermediate scales  $\alpha_s(M_Z) \approx 0.118$ , the interactions at high-energy hadron colliders can be treated perturbatively in  $\alpha_s$ . For any process cross-section  $\sigma_{ab \rightarrow X}$ , where  $a$ ,  $b$ , and  $X$  are freely propagating initial-, respectively final-states, one can expand the matrix-element in a Taylor series,

$$\hat{\sigma}_{ab \rightarrow X} = \alpha_s^k(\mu_R^2) (\hat{\sigma}_{\text{LO}}(p_i, p_f; \mu_R^2) + \alpha_s(\mu_R^2) \hat{\sigma}_{\text{NLO}}(p_i, p_f; \mu_R^2) + \mathcal{O}(\alpha_s^2(\mu_R^2)) + \dots) \quad (3.12)$$

At each order in the strong coupling  $\alpha_s$ , the cross-section can be computed and will depend on the choice of the renormalization scale. Usually it is chosen close to the expected momentum exchange  $Q^2$ . The systematic uncertainty related to the arbitrary choice of the scale is then estimated by varying the renormalization scale by factors of  $\frac{1}{2}$  and 2.

The accuracy of a computation is given by the truncation order of the perturbative series in Eq. (3.12). In certain regions of phase-space, though, large prefactors can be introduced at all orders, when two far-away scales  $Q$  and  $q$  are involved. This usually spawns the appearance of large logarithms of the form  $\ln^\alpha(Q^2/q^2)$ , which have to be

### 3 Higher-order calculations in hadron-hadron collisions

resummed to a given *logarithmic* accuracy across all orders. Some details will be given in Section 4.2.

## 3.2 Infrared divergences

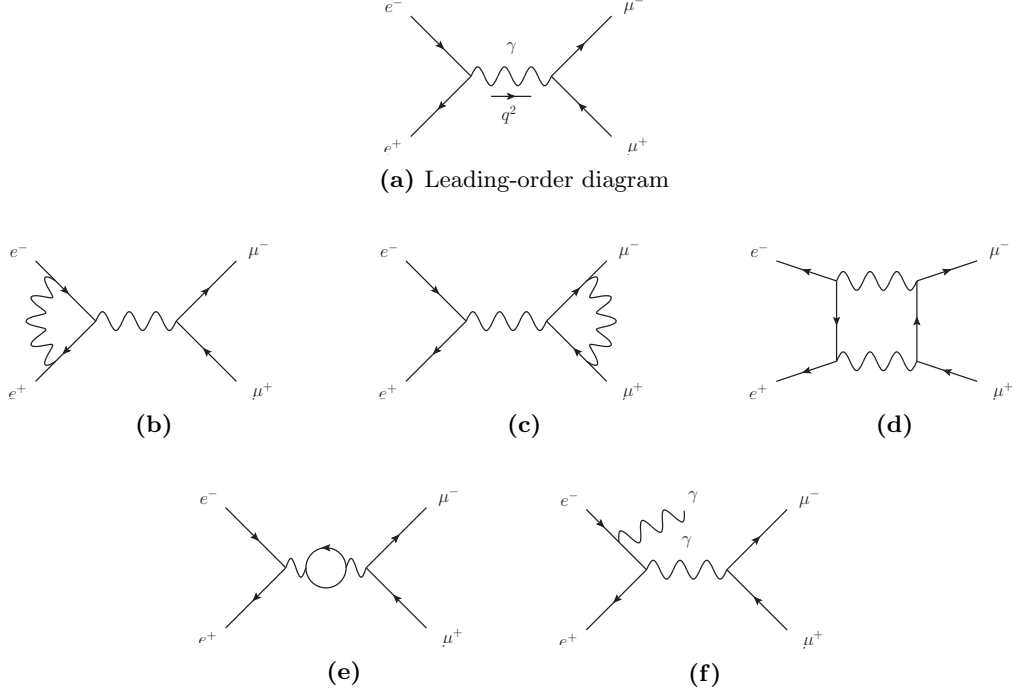


**Figure 3.2:** Feynman diagrams for  $e^+e^- \rightarrow \mu^+\mu^-$ . (a) The only leading-order diagram, with a photon in the  $s$ -channel (b-e) Virtual one-loop corrections. (f) Real-emission diagram

Starting from an example, let's consider the case of QED higher-order corrections to  $e^+e^- \rightarrow \mu^+\mu^-$  annihilation. Feynman diagrams up to  $\mathcal{O}(\alpha^3)$  are shown in Fig. 3.2. At leading-order, the cross-section is given by

$$\sigma_{\text{LO}} = \int_{\Phi} d\Phi |\mathcal{M}_0|^2 = \frac{4\pi\alpha^2}{3q^2} \quad (3.13)$$

with  $q^2$  the momentum carried by the exchanged photon, and the squared amplitude  $|\mathcal{M}_0|^2$  has to be integrated over the phase-space  $\Phi$ . Let's assume the UV divergences have been handled by the introduction of appropriate counterterms. That is, the UV divergences stemming from the loop momentum integration from diagrams (b) and (c) in Fig. 3.2 have been taken care of by renormalizing the electron charge and the muon charge, respectively. Diagram (e) is also UV divergent but is nothing else than vacuum polarization in QED (thus, it has no impact on any observable), while diagram (d) has

531 no UV divergence. Computing the amplitude, one realizes there is also an IR divergence  
 532 coming from the massless photon propagator in the loops.

533 First, the IR divergence needs regularizing. The simplest way to do that is to give the  
 534 photon a small, non-zero mass,  $m_\gamma > 0$ , and to take the limit  $m_\gamma \rightarrow 0$  at the end of the  
 535 calculation. Computing the virtual contribution,  $\sigma_V \propto (\mathcal{M}_V^\dagger \mathcal{M}_0 + \text{h.c.})$ , one arrives  
 536 at the result

$$\sigma_V = \frac{2}{3} \pi^2 \frac{\alpha^3}{q^2} \left( \frac{\pi^2}{5} - \frac{7}{2} - \ln^2 \left( \frac{m_\gamma^2}{q^2} \right) - 3 \ln \left( \frac{m_\gamma^2}{q^2} \right) \right). \quad (3.14)$$

537 The IR divergence is still present but it is explicit in  $\ln(m_\gamma)$ .<sup>3</sup> For the perturbative  
 538 expansion to be consistent, we have to include real-emission diagrams of  $\mathcal{O}(\alpha^3)$ , that is  
 539 diagrams of the sort pictured in Fig. 3.2f, where a photon is radiated either from the  
 540 initial- or the final-state. Doing so, one gets a contribution of the form  $\sigma_R \propto |\mathcal{M}_R|^2$ :

$$\sigma_R = \frac{2}{3} \pi^2 \frac{\alpha^3}{q^2} \left( -\frac{\pi^2}{5} + 5 + \ln^2 \left( \frac{m_\gamma^2}{q^2} \right) + 3 \ln \left( \frac{m_\gamma^2}{q^2} \right) \right). \quad (3.15)$$

541 Combining the different contributions to the cross-section, the IR divergences can-  
 542 cel between the virtual one-loop and the real-emission matrix-elements to give a finite  
 543 correction to the leading-order:

$$\sigma_{\text{NLO}} = \sigma_{\text{LO}} + \sigma_V + \sigma_R = \sigma_{\text{LO}} \left( 1 + \frac{3}{4\pi} \alpha \right) \quad (3.16)$$

544 This behaviour is symptomatic of IR divergences and falls under the purview of the  
 545 Kinoshita–Lee–Nauenberg (KLN) theorem, which states that sufficiently inclusive ob-  
 546 servables are always IR-finite.

547 Although the cancellation of IR divergences is ensured by the KLN theorem, it is  
 548 non-trivial to realize it numerically (for example in the context of a Monte-Carlo event  
 549 generator). Section 4.1.2 will briefly develop this point.

### 550 3.3 The factorization theorem

551 Because the collision of composite states like the protons used at LHC implies inter-  
 552 actions of highly non-perturbative objects, it is not clear at first how to handle these  
 553 theoretically: color confinement does not allow for free quarks or gluons to be observed,  
 554 thus the initial-state in hadron colliders cannot a priori be defined perturbatively. At  
 555 high-energy, though, we can make use of the fact that the interaction with the highest  
 556 momentum exchange takes place over time scales that are far smaller than the typical  
 557 time scale at which the proton's constituents interact among themselves. The description  
 558 of such a collision can therefore be *factorized* in long- and short-distance (or short- and

---

<sup>3</sup>The divergent terms are called Sudakov double logarithms and are systemic of collinear/soft emission (see Chapter 4).

### 3 Higher-order calculations in hadron-hadron collisions

long-time scale) physics: a hard collision of two partons, respectively non-perturbative interactions within hadrons. Mathematically, the cross-section  $\sigma_{pp \rightarrow X}$  for the production of a state  $X$  from the collision of two protons can be written as

$$\sigma_{pp \rightarrow X} = \sum_{ab} \int dx_a f_{a/p}(x_a, \mu_F^2) \int dx_b f_{b/p}(x_b, \mu_F^2) \cdot \hat{\sigma}_{ab \rightarrow X}(x_a p_1, x_b p_2; \mu_F^2) \quad (3.17)$$

where  $a$  and  $b$  are possible constituents of the parent protons (sea or valence quarks and gluons),  $f_{a/p}$ ,  $f_{b/p}$  are encoding the non-perturbative origin of the partons in the parent protons, and  $\hat{\sigma}_{ab \rightarrow X}$  is the cross-section for the production of the final-state  $X$  from the collision of the free partons  $a$  and  $b$ , the latter of which can now be computed perturbatively in QCD. Eq. (3.17) is called the *factorization theorem* of Quantum Chromodynamics, and sets the basis for all cross-section predictions at LHC. The functions  $f_{a/p}$ ,  $f_{b/p}$ , which are called *parton distribution functions* (PDF), depend on the momentum fraction  $\xi_a$ ,  $\xi_b$  carried away by the parton from the parent proton, and on the resolution scale  $Q^2$ . Crudely said, the partonic content of the protons depends on the scale at which they are resolved.<sup>4</sup> The PDFs by definition cannot be computed perturbatively in QCD, but they can be measured from experimental data. As a matter of fact, a precise measurement of the proton's PDF is crucial, and constitutes one of the main sources of uncertainty in theoretical predictions at the LHC. Fig. 3.3 depicts the measurement of the proton PDFs by the MSTW collaboration from a global fit of hard-scattering data [20].

---

<sup>4</sup>The PDFs also obey an evolution equation similar to the RGE called DGLAP equation: this evolution runs from a central scale choice, namely the *factorization scale*  $\mu_F$ .

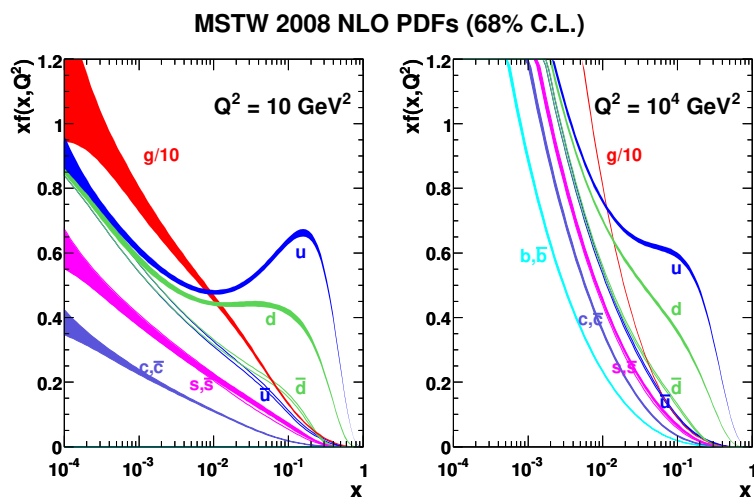


**Figure 3.3:** The MSTW 2008 NLO proton PDFs [20] as a function of the parent proton's momentum fraction  $x$  at resolution scales  $Q^2 = 10 \text{ GeV}^2$  (left),  $Q^2 = 10^4 \text{ GeV}^2$  (right)



## <sup>577</sup> 4 Monte-Carlo event generators

<sup>578</sup> To be able to compare a theory prediction for hadron colliders to an experimental mea-  
<sup>579</sup> surement released by e.g. the ATLAS experiment, theorists and experimentalists meet  
<sup>580</sup> on a common ground: the event rate  $\sigma$ . The event rate can be an inclusive cross-section,  
<sup>581</sup> like the total rate of events after applying cuts and correcting for the detector accep-  
<sup>582</sup> tance, or it can be a differential cross-section with respect to some kinematic variable  
<sup>583</sup>  $d\sigma/d\mathcal{O}$ , where  $\mathcal{O} = n_{\text{jets}}, m_{t\bar{t}}, \dots$  is any event observable. On one side, the theorists  
<sup>584</sup> need to compute a cross-section from a QFT starting point, namely the Lagrangian: at  
<sup>585</sup> the most basic level, this means implementing Fermi's golden rule (Eq. (4.1)). On the  
<sup>586</sup> other side, experimentalists have to count events and correct for detector acceptance  
<sup>587</sup> and resolution (Eq. (4.2)):

$$\sigma = \frac{1}{4E_a E_b v} \int \prod_f \left( \frac{d^3 p_f}{(2\pi)^3} \frac{1}{2E_f} \right) |\mathcal{M}_{fi}|^2 (2\pi)^4 \delta^4(p_a + p_b - \sum_f p_f) \quad (4.1)$$

$$\sigma = \frac{N_{\text{events}}}{\epsilon \cdot \mathcal{L}_{\text{int}}} \quad (4.2)$$

<sup>588</sup> where  $E_a$  and  $E_b$  are the energies of the incoming particles  $a$  and  $b$ , the flux per unit  
<sup>589</sup> volume  $v = |\vec{v}_a - \vec{v}_b|$  is given by the relative 3-velocities of the particles and  $p_f$ ,  $E_f$  are  
<sup>590</sup> the 3-momenta and energies of all final states. As a matter of fact, the infinitesimal  
<sup>591</sup> volume element above is relativistically invariant. Ultimately, the relativistic matrix-  
<sup>592</sup> element squared  $|\mathcal{M}_{fi}|^2$  has to be integrated over the whole phase-space while enforcing  
<sup>593</sup> 4-momentum conservation. Experimentally, in Eq. (4.2), the cross-section is equal to the  
<sup>594</sup> event count, corrected for phase-space acceptance, detector resolution and normalized  
<sup>595</sup> by the instantaneous luminosity  $\mathcal{L}_{\text{int}}$ . For the case of differential distributions, the  
<sup>596</sup> formula becomes more complicated, as binned events migrate depending on the detector  
<sup>597</sup> resolution. The discussion of this case is postponed to Chapter 8.

<sup>598</sup> There are two issues with the picture at hand. First, the matrix-element for a given  
<sup>599</sup> process can typically be computed up to  $\mathcal{O}(\text{few})$  external legs. Because the multiplicity  
<sup>600</sup> of final-state particles in a collider experiment like the LHC is of the order  $\mathcal{O}(10^2 - 10^3)$ , it  
<sup>601</sup> is virtually impossible to calculate such amplitudes. Second, the perturbative expansion  
<sup>602</sup> presented in Chapter 3 breaks down when colored particles are produced with small  
<sup>603</sup> energies. In particular, around energy scales where free final-state partons fall in the  
<sup>604</sup> realm of non-perturbative interactions, they hadronize to form the observable colorless  
<sup>605</sup> bound states demanded by color confinement. Therefore, the structure of the whole  
<sup>606</sup> collision has to be broken down into pieces across the several scales involved, and the  
<sup>607</sup> theoretical treatment of each piece is valid only in these subdomains and subjected  
<sup>608</sup> to different levels of approximations. The theory community developed the necessary

## 4 Monte-Carlo event generators

609 ingredients to improve the description of each stage and assembled them into mostly-  
 610 automated programs called *Monte-Carlo (MC) event generators*.

611 MC event generators basically simulate the particle collisions as they would happen  
 612 at the interaction points of an experiment like ATLAS and CMS. A typical MC event is  
 613 pictured in Fig. 4.1.

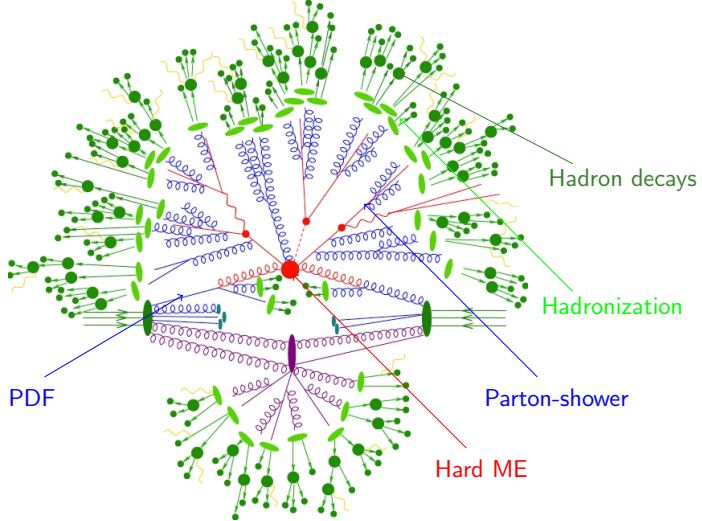


**Figure 4.1:** A Monte-Carlo event generator matches multi-scale physics to simulate a collision, taking into account non-perturbative (PDF and quark fragmentation, hadron decay, underlying event, proton beam remnants) as well as perturbative (matrix-element and parton-shower matching) phenomena.

614 Under the hood of any Monte-Carlo program, the ingredients are essentially the same:

- 615 • **Monte-Carlo integrator:** the phase-space is sampled, usually with the help of an  
 616 adaptive Monte-Carlo integration algorithm, to numerically perform the integral  
 617 given in Eq. (4.1). As a notable example, the `Cuba` library [21] implements four  
 618 multi-dimensional integration algorithms: `Vegas`, `Divonne`, `Suave` and `Cuhre`.
- 619 • **PDFs:** there is an extensive amount of PDF measurements varying in the used  
 620 datasets, theoretical precision, combination strategy, handling of  $\alpha_s$ , or flavour  
 621 thresholds. The `LHAPDF` package [22] interpolates PDF values from discrete mea-  
 622 surement points in the  $(x, Q^2)$  phase-space and can be interfaced to the MC gen-  
 623 erator.
- 624 • **Hard matrix-element:** the core of the calculation is the computation of the  
 625 matrix-element  $\mathcal{M}_{fi}$ . It determines the theoretical accuracy of the prediction to a  
 626 given order in  $\alpha_s$ . More details are given in Sec. 4.1.

- **Parton shower:** as stated above, the high-multiplicity endstate is evolved from the few-parton hard matrix-element through subsequent radiative emission by a parton-shower algorithm. These routines base on first-principles QCD (and QED), but contain inherent approximations and parametric degrees of freedom that generate an uncertainty associated with the choice of algorithm. Section 4.2 will expand on the topic.
- **Hadronization and hadron decay:** once the shower evolution is brought down to energies of the order of the hadronization scale (around  $\mathcal{O}(1 \text{ GeV})$ ), the free partons bind to form colorless states. This is handled by a model on the only assumption that it should describe data to the best possible extent. Commonly, these models have a certain number of free parameters that are *tuned* to data. In Sec. 4.3, the Lund string and the cluster model are briefly detailed.
- **Multiple partonic interaction and underlying event:** especially at small momentum fractions, it is possible that more than one parton from the same parent proton contributes to the interaction. The description of this phenomenon is also mostly based on MC modeling and has to be tuned to experimental data.

## 4.1 Matrix-element providers

The first programs for generating the matrix-element  $\mathcal{M}_{fi}$  needed in Eq. (4.1) were highly specialized. They would handle one specific process and would be mostly analytically hard-coded. At some point, authors from the theory community started to make their code available and the corresponding libraries would be assembled into multi-processes packages. This is the example of the NLOJet++ [23] and MCFM [24] packages. Nowadays, after a paradigm shift, the computation of the hard process matrix-element is decidedly automatized at one-loop level: programs like MADGRAPH [25], OPENLOOPS [26, 27] and GoSAM [28, 29] can be interfaced directly to most MC generators and provide the amplitude given any phase-space point, while other programs focus on specific processes, as for example NJET [30], which calculates multijet amplitudes at NLO in massless QCD, VBFNLO [31, 32, 33] for vector-boson fusion in a number of processes, or HJETS++ [34] for Higgs boson production in association with one or more jets. We use GoSAM-2.0 in all subsequent NLO computations, thus the mode of operation of the program is detailed in the next Section.

### 4.1.1 GoSam: computation of one-loop amplitudes

GoSAM is a general-purpose package that computes one-loop amplitudes automatically and interfaces to any MC generator, provided it supports the Binoth-Les Houches Accord (BLHA1 [35] or BLHA2 [36]) format. The working flow of GoSAM is shown in Fig. 4.2. Any process can be defined in the GoSAM input card, where only incoming and outgoing particles as well as the desired order in  $\alpha, \alpha_s$  for the generation of the Feynman diagrams have to be given. The PYTHON `gosam.py` executable is then called and a series

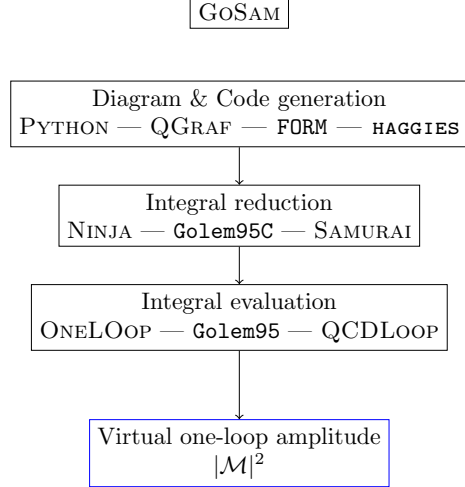


**Figure 4.2:** GoSAM relies on external packages to compute virtual one-loop amplitudes. Feynman diagrams are generated (and drawn) by QGRAF, and fortran code containing the terms relevant to each diagram is automatically written out in FORM. The various integral families are then reduced by either NINJA, Golem95C or SAMURAI libraries. Finally, the basis integrals are evaluated using either the ONELOOP, Golem95C or QCDLOOP packages.

of external packages handle the different steps of the computation: QGRAF [37] generates the Feynman diagrams, and filters for vertices or propagators can be applied, as well as manual removal of diagrams. Then, FORM [38] code containing the relevant expressions is generated automatically for all diagrams and helicities. Integral reduction is operated by any of three programs, namely NINJA [39], Golem95C [40, 41] or SAMURAI [42]. Finally, the evaluation of the set of basis integrals is checked out in external integral repositories, either QCDLOOP [43], ONELOOP [44] or Golem95C.

On a higher level, according to the BLHA, the MC generator produces a contract file containing the subprocesses to be computed by GOSAM. The latter is called and generates routines for all subprocesses, libraries for all helicities are linked, and common functions are written in a `matrix.f90` file to be called by the MC generator. The physics parameters, like particles masses and couplings, can be set by an external call to the `OLP_Option` function. Then, for a set of 4-momenta  $(p_i^\mu)_{i=1,\dots,n}$ , the matrix-element is provided by calling the `OLP_EvalSubProcess((p_i^\mu)_{i=1,\dots,n})` function, which returns the full 1-loop amplitude coefficients (double, single pole and finite terms) as given in the Laurent series

$$|\mathcal{M}|^2 = \frac{\alpha_s}{2\pi} \frac{(4\pi)^\epsilon}{\Gamma(1-\epsilon)} \left( \frac{c_{-2}}{\epsilon^2} + \frac{c_{-1}}{\epsilon} + c_0 + \mathcal{O}(\epsilon) \right) \quad (4.3)$$

GOSAM is a very flexible package, and allows high-level control over the various subtleties of higher-order computations (e.g. choice of regularization scheme, renormalization counterterms, and so on). A rescue system for phase-space points that are numer-

684 ically badly behaved can be activated, and the amplitude for these is recomputed in  
 685 quadruple precision.

### 686 4.1.2 Infrared divergence cancellation

687 Going beyond the virtual contribution to the amplitude, one has to combine the Born,  
 688 virtual and real-emission contributions together. As was shown in Section 3.2, the sin-  
 689 gularities appearing in both virtual loop calculations and in soft/collinear configura-  
 690 tions of real emissions should combine to give finite quantities for any IR-safe observable.<sup>1</sup>  
 691 Although this is analytically true, in the case of MC computations, the different contri-  
 692 butions are first sampled over different phase-spaces, then combined. Symbolically, we  
 693 have:

$$\sigma^{\text{NLO}} = \int_{\Phi_m} d\sigma^B + \int_{\Phi_m} d\sigma^V + \int_{\Phi_{m+1}} d\sigma^R, \quad (4.4)$$

694 where the singularities in virtual and real contributions only cancel after integration.  
 695 Numerically, the cancellation of IR divergences is thus non-trivial. At NLO, there are  
 696 two kinds of algorithms to implement IR divergence cancellation: phase-space slicing and  
 697 subtraction methods. The Catani-Seymour automatized subtraction of IR divergences  
 698 is mostly used nowadays in NLO MC generators. The algorithm is outlined below and  
 699 is used in all calculations present from Chapter 6 on.

700 Consider the addition of a subtraction term which approximates the ( $d = 4 - 2\epsilon$   
 701 regularized) real contribution and reproduces its divergence pattern in  $d$  dimensions:

$$d\sigma^V + d\sigma^R = d\sigma^V + d\sigma^S + (d\sigma^R - d\sigma^S). \quad (4.5)$$

702 Then, the ( $d = 4$ )-dimension limit can be taken directly for the real integration and  
 703 the local counterterm cancels the divergence in the phase-space integrand. The same  
 704 is true for the virtual contribution, in general, only after integration. Returning to the  
 705 phase-space integrated result, the total NLO cross-section takes the form:

$$\sigma^{\text{NLO}} = \int_{\Phi_m} d\sigma^B + \int_{\Phi_m} \left( d\sigma^V + \int_{\Phi_1} d\sigma^S \right)_{\epsilon=0} + \int_{\Phi_{m+1}} (d\sigma^R|_{\epsilon=0} - d\sigma^S|_{\epsilon=0}), \quad (4.6)$$

706 where both of the last integrals are now separately finite. The Catani-Seymour dipole  
 707 formalism is a factorization formula that allows the automatic generation of the subtrac-  
 708 tion term  $d\sigma^S$ . Universal dipole factors are introduced for any process, and setting the  
 709 subtraction term to

---

<sup>1</sup>Generally, at NLO, regularized poles thus appear either as double poles (soft and collinear), or single poles (soft, collinear, or UV).

$$d\sigma^S = \sum_{\text{dipoles}} d\sigma^B \otimes dV^{\text{dip.}}, \quad (4.7)$$

$$\int_{\Phi_{m+1}} d\sigma^S = \sum_{\text{dipoles}} \int_{\Phi_m} d\sigma^B \otimes \int_{\Phi_1} dV_{\text{dip.}} =: \int_{\Phi_m} d\sigma^B \otimes \mathbf{I} \quad (4.8)$$

710 allows one to compute the cross-section  $\sigma^{\text{NLO}}$  of any process:

$$\int_{\Phi_m} d\sigma^B + \int_{\Phi_m} (d\sigma^V + d\sigma^B \otimes \mathbf{I})_{\epsilon=0} + \int_{\Phi_{m+1}} \left( d\sigma^R|_{\epsilon=0} - \sum_{\text{dipoles}} d\sigma^B \otimes dV_{\text{dip}}|_{\epsilon=0} \right) \quad (4.9)$$

711 with  $\mathbf{I}$  the integrated CS insertion operator. The universal dipole factors are obtained  
 712 by considering the soft/collinear limits of a one-emission matrix-element with respect to  
 713 the Born configuration:

$$|\mathcal{M}_{m+1}|^2 = \sum_{k \neq i,j} \mathcal{D}_{ij,k}(p_1, \dots, p_{m+1}) + (\text{regular in } p_i \cdot p_j \rightarrow 0) \quad (4.10)$$

$$= - \sum_{k \neq i,j} \frac{1}{2p_i \cdot p_j} \mathcal{M}_m^\dagger(i, j \rightarrow \tilde{i}\tilde{j}, \tilde{k}) \left( \frac{\mathbf{T}_k \cdot \mathbf{T}_{ij}}{\mathbf{T}_{ij}^2} \mathbf{V}_{ij,k} \right) \mathcal{M}_m(i, j \rightarrow \tilde{i}\tilde{j}, \tilde{k}) \\ + (\text{regular in } p_i \cdot p_j \rightarrow 0) \quad (4.11)$$

714 where the singular terms are collected in the dipoles  $D_{ij,k}$ . The  $\mathbf{T}_i$  are the generators of  
 715 the colour algebra and  $\mathcal{M}_m$  is a general matrix-element corresponding to an  $m$ -particle  
 716 final-state,  $\mathcal{M}_m = |1, \dots, m\rangle$ . Then Eq. (4.11) states that the matrix-element corre-  
 717 sponding to an  $(m+1)$ -particle final-state factorizes into dipole factors  $\mathbf{V}_{ij,k}$  convoluted  
 718 with an underlying Born configuration where partons  $i$  and  $j$  are assembled into one  
 719 parton  $(\tilde{i}\tilde{j})$  (the so-called *emitter*), and parton  $\tilde{k}$  (the *spectator*) absorbs the residual  
 720 4-momentum. The formulae for the universal dipoles  $\mathbf{V}_{ij,k}$  are very closely related to  
 721 the Altarelli-Parisi splitting functions, see Section 4.2.

722 In the case of the presence of initial-state hadrons like at the LHC, Eq. (4.11) is  
 723 modified and an additional dipole term has to be added in Eq. (4.8),  $dV_{\text{dip}} \rightarrow dV_{\text{dip}} +$   
 724  $dV'_{\text{dip}}$ . Eq. (4.8) then becomes

$$\int_{\Phi_{m+1}} d\sigma^S = \int_{\Phi_m} d\sigma^B \otimes \mathbf{I} + \int_0^1 dx \int_{\Phi_m} d\sigma_B(xp) \otimes (\mathbf{P} + \mathbf{K})(x), \quad (4.12)$$

725 where  $xp$  is the proton momentum fraction carried away from the hadron, and  $\mathbf{P}, \mathbf{K}$   
 726 are insertion operators appearing from the convolution with the PDF.

## 4.2 Parton-shower models

### 4.2.1 Altarelli-Parisi splitting functions

Inherently, the few-parton, high-energy final-state generated by the hard process matrix-element further produces both QCD and QED radiation. The parton-shower algorithm evolves partons from the collision scale  $Q^2$  to a cutoff scale  $Q_{\min}^2$  that is set around the hadronization scale. At that point, the shower terminates and the final-state is passed on to the hadronization model. Schematically, the shower algorithm is based on the so-called Dokshitzer–Gribov–Lipatov–Altarelli–Parisi (DGLAP) kernels [45, 46, 47] for  $1 \rightarrow 2$  collinear particle splitting  $P_{a \rightarrow bc}$ , as given in Fig. 4.3.

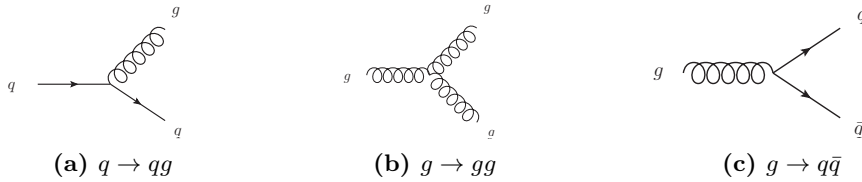


**Figure 4.3:** The QCD vertices for  $1 \rightarrow 2$  splittings allow to calculate the leading-order kernels appearing in the DGLAP evolution equation.

The (unregularized) LO kernels can be computed from the QCD interaction vertices as:

$$P_{q \rightarrow qg}(z) = C_F \frac{1 + z^2}{1 - z} \quad (4.13)$$

$$P_{g \rightarrow gg}(z) = 2C_A \left( \frac{1 - z}{z} + z(1 - z) + \frac{z}{1 - z} \right) \quad (4.14)$$

$$P_{g \rightarrow q\bar{q}}(z) = T_R(1 - 2z(1 - z)) \quad (4.15)$$

with  $z$ ,  $0 \leq z \leq 1$  the longitudinal momentum fraction of the parent parton  $a$ . Notice the undefined behaviour of  $P_{q \rightarrow qg}$  and  $P_{g \rightarrow gg}$  for  $z = 1$ . The splitting functions can be regularized from general constraints to:

$$P_{q \rightarrow qg}(z) = C_F \left( \frac{1 + z^2}{(1 - z)_+} + \frac{3}{2} \delta(z - 1) \right) \quad (4.16)$$

$$P_{g \rightarrow gg}(z) = 2C_A \left( \frac{1 - z}{z} + z(1 - z) + \frac{z}{(1 - z)_+} + \left( \frac{11}{12} - \frac{1}{3} \frac{T_R}{C_A} \right) \delta(z - 1) \right) \quad (4.17)$$

$$P_{g \rightarrow q\bar{q}}(z) = T_R(1 - 2z(1 - z)) \quad (4.18)$$

The factor  $(1 - z)^{-1}$  is regularized in being interpreted as a plus-distribution  $(1 - z)_+^{-1}$  such that for any test function  $f(z)$  sufficiently regular at  $z = 0, z = 1$ ,

$$\int_0^1 \frac{dz f(z)}{(1-z)_+} = \int_0^1 \frac{f(z) - f(1)}{1-z} dz \quad (4.19)$$

743     The master equation governing the evolution of the collinear splitting of a parton  $a$   
 744     from a scale  $q^2$  to a scale  $q^2 + dq^2$  is then given by

$$dP_{a \rightarrow bc} = \frac{dq^2}{q^2} \frac{\alpha_s}{2\pi} P_{a \rightarrow bc}(z) dz \quad (4.20)$$

745     where  $q^2$  is an arbitrary strong-ordered evolution variable. It can be the azimuthal  
 746     angle of emission  $E_a^2 \theta^2$ , or the particle's virtuality  $m^2$ , or the transverse momentum  
 747      $p_T^2$ . Different shower algorithms implement different choices of the evolution variable.  
 748     This will be of importance when considering parton-shower related uncertainties, see  
 749     Chapters 7 and 11.

### 750     4.2.2 The Sudakov form factor

751     Going from the one-emission to the multiple-emission case, and using broad assump-  
 752     tions<sup>2</sup>, the probability of no-emission between scales  $Q^2$  and  $Q_{\max}^2$  is given by the *Sudakov*  
 753     form factor:

$$dP_{a \rightarrow bc}(z) = \frac{dq^2}{q^2} \frac{\alpha_s}{2\pi} P_{a \rightarrow bc}(z) dz \times \exp \left( - \sum_b \int_{Q^2}^{Q_{\max}^2} \frac{dq'^2}{q'^2} \int \frac{\alpha_s}{2\pi} P_{a \rightarrow bc}(z') dz' \right) \quad (4.21)$$

754     As explained in Sec. 3.1.3, the perturbative expansion of the cross-section in  $\alpha_s$  can  
 755     suffer from large enhancements in the soft/collinear regions of phase-space. In general,  
 756     double logarithms of the form  $\alpha_s^n \log^{2n}(Q^2/q^2)$  appear when a soft particle is emitted, or  
 757     when it becomes collinear to one of the incoming partons. Here,  $q^2$  is the scale describing  
 758     the soft/collinear emission, and  $Q^2$  is the global scale of the process. Generally, this tower  
 759     of large logarithms can be analytically resummed to all orders in  $\alpha_s$ . Instead, the parton  
 760     shower algorithm offers the possibility of resumming soft and collinear contributions  
 761     within the Monte-Carlo framework. Nowadays, most parton showers only guarantee  
 762     leading-logarithmic (LL) accuracy, although recent studies [48] have found differences at  
 763     LL (subleading number of colors  $N_c$ ), and NLL (leading- $N_C$ ) between parton-showers  
 764     and analytic resummations.

### 765     4.2.3 Parton-shower matching

766     The shower algorithm should respect the theoretical accuracy of the hard matrix-element,  
 767     and at the same time conserve the logarithmic accuracy of the parton-shower resumma-  
 768     tion in their respective limits. In particular, the cross-section after showering should

---

<sup>2</sup>Namely that the time between emissions can be sliced, and unitarity as well as multiplicativity (meaning the shower has no memory of past emissions) hold.

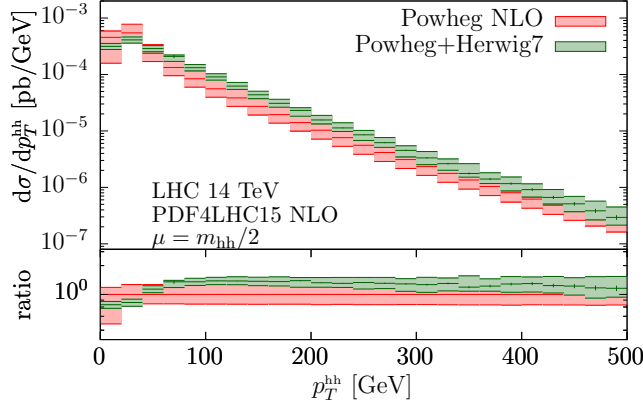


**Figure 4.4:** The transverse momentum  $p_T(hh)$  in di-Higgs production is compared for the fixed-order NLO prediction to a parton-shower matched calculation. The parton-shower correctly reproduces the NLO computation at high-transverse momentum and softens the low-momentum region (Sudakov suppression).

be identical to the fixed-order cross-section. Also, kinematic configurations that belong both to the hard matrix-element and the parton-shower final-states should not be double-counted. This whole procedure is called *matching*. At NLO, the matching of the parton-shower algorithm to the fixed-order matrix-element handles both these issues. Roughly said, it interpolates between the two kinematic regions where the hard matrix-element, respectively the parton-shower, generate their respective dominant contributions. An illustration of this fact is shown in Fig. 4.4 for the case of  $gg \rightarrow HH$  production, where an NLO calculation is matched to the **Herwig7** [49, 50] parton-shower. Among the various matching procedures that keep in line with the above criteria, the subtractive MC@NLO [51] and the multiplicative Powheg [52] schemes are among the most used ones.

As examples of available parton-shower algorithms, the **Pythia** [53, 54] and **Herwig** codes implement a  $p_T$ -ordering, respectively an angular-ordering in the choice of the evolution variable. **Herwig** also uses a dipole shower as an alternative algorithm (which is based on a Catani-Seymour dipole formulation of  $2 \rightarrow 3$  splitting kernels). The **Sherpa** [55] generator implements two alternative parton-shower algorithms based on variations of the CS dipoles.

### 4.3 Hadronization

Once particles have been showered down to the hadronization scale, the hadronization model takes over. By far, the two most used hadronization models are the Lund string model and the cluster model.

790 **4.3.1 Lund string model**

791 The Lund string model [56] bases on the principle of quark color confinement. When  
 792 two quarks with electric charges  $q_1, q_2$  are separated by a distance  $r$ , the potential takes  
 793 the form:

$$U(r) = -\frac{q_1 q_2}{r} + \kappa r \quad (4.22)$$

794 and the linear confinement contribution dominates for larger distances, with  $\kappa \sim$   
 795 1 GeV/fm. In analogy to a classical elastic potential, the field lines build up a stretched  
 796 *string*. When the distance between a quark-pair increases, the string tension grows until  
 797 it breaks: the freed energy creates another quark-antiquark pair appearing from the  
 798 vacuum. This is pictured in Fig. 4.5a. The creation of the quark-pair happens with a  
 799 Gaussian probability (similarly to quantum tunnelling) in the quark transverse mass  $m_T^2$ .  
 800 From Lorentz invariance, causality and left-right symmetry, the fragmentation function  
 801  $f(z)$  can be constrained and fixes the longitudinal momentum fraction  $z$  carried away  
 802 by the created hadron:

$$\mathcal{P} \propto \exp\left(-\frac{\sigma m_T^2}{\kappa}\right), \quad f(z) \propto \frac{(1-z)^a}{z} \exp\left(-\frac{bm_T^2}{z}\right) \quad (4.23)$$

803 The Lund string model is implemented in the **Pythia** generator and the main parameters  
 804  $a, b, \sigma$  are determined by tuning to data. For the more complex case of baryons,  
 805 the three quarks can be pictured in a quark-diquark frame. Finally, the gluons appear  
 806 as kinks on strings. Flavour-suppression for strange quarks is also handled by an ad-  
 807 ditional parameter. For more details and improvements to the model, see the **Pythia**  
 808 manual [57].

809 **4.3.2 Cluster model**

810 Instead of building on color confinement, the cluster model [58, 59] makes the assumption  
 811 that gluons can be viewed as carrying color and anticolor and behaving as a  $q\bar{q}$  pair.  
 812 Color singlets usually obey a mass spectrum that peaks at low mass due to the property  
 813 of preconfinement of the parton shower [60], i.e. they are closer to one another in phase  
 814 space. The model then clusters these color singlets together and splits them per the  
 815 following procedure: if a cluster of mass  $M$ , with parton constituents of masses  $m_1, m_2$ ,  
 816 satisfies

$$M^{C_{\text{pow}}} > C_{\text{max}}^{C_{\text{pow}}} + (m_1 + m_2)^{C_{\text{pow}}}, \quad (4.24)$$

817 the algorithm splits it and the masses get redistributed. To split a cluster, the model  
 818 pops a  $q\bar{q}$  pair from vacuum and forms two new clusters with one original parton each,  
 819 and masses distributed according to

$$M_{1,2} = m_{1,2} + (M - m_{1,2} - m_q) \mathcal{R}_{1,2}^{P_{\text{split}}}, \quad (4.25)$$

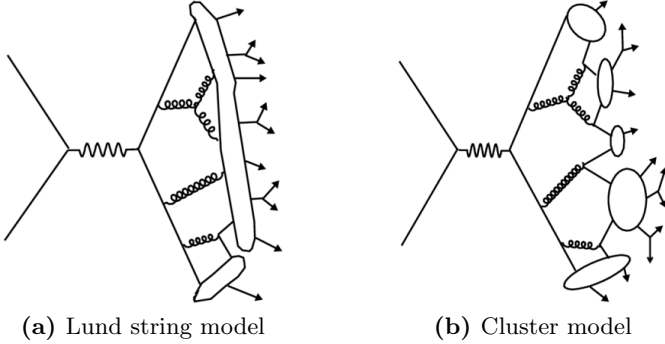


**Figure 4.5:** A pictorial representation of both hadronization models. (a) In the Lund model, the potential energy from the color field between two quarks increases linearly with the distance, like in a string. When a string breaks, a new quark-antiquark pair is created. (b) The **Herwig** model groups color-connected partons together into clusters and lets them decay isotropically.

820 with  $\mathcal{R}_{1,2} \in [0, 1]$  two random numbers. Again, the parameters  $C_{\text{pow}}$ ,  $C_{\text{max}}$  and  $P_{\text{split}}$   
821 have to be tuned to data.

822 Notice that the cluster model does not propagate any spin information: the hadronized  
823 clusters therefore decay isotropically. Historically, the cluster model was implemented in  
824 the **Herwig** event generator. Fig. 4.5b summarizes the conceptual differences between the  
825 Lund string and the cluster model. As a concluding remark, the MC event generators  
826 represent the basis of a large fraction of experimental measurements. As such, they  
827 are quite complex systems whose constituents are all correlated together: the different  
828 pieces interact and the matching between all appearing physical scales is not always  
829 explicit at the end of the simulation. Finally, variations in the MC setup are linked  
830 to large uncertainties which should, in principle, be taken into account with their full  
831 correlations.



## <sup>832</sup> 5 The LHC and the ATLAS detector

<sup>833</sup> The Large Hadron Collider, or LHC, is currently the most powerful particle accelerator  
<sup>834</sup> worldwide and is located at the Centre Européen pour la Recherche Nucléaire (CERN)  
<sup>835</sup> on the French-Swiss border, near Geneva. Historically, it replaced the Large Electron-  
<sup>836</sup> Positron (LEP) collider after it was decommissioned in 2000, and is being housed in  
<sup>837</sup> the same tunnel. In this Chapter, we shall briefly review the main working parts of  
<sup>838</sup> the accelerator complex, and then dive in more detail into the structure of the ATLAS  
<sup>839</sup> detector. A short overview of the trigger system and data acquisition will close the  
<sup>840</sup> subject.

### <sup>841</sup> 5.1 The Large Hadron Collider

<sup>842</sup> The LHC's main collider ring is installed in a circular tunnel of  $\sim 27$  km circumference  
<sup>843</sup> and a depth varying between 45 m and 170 m under ground level. It is designed to  
<sup>844</sup> accelerate protons to a design center-of-mass energy of 14 TeV at a peak luminosity  
<sup>845</sup> of  $10^{34} \text{ cm}^{-2} \text{ s}^{-1}$ . As a side note, the LHC also collides heavy ions, and in the past a  
<sup>846</sup> few runs of lead-lead, proton-lead and xenon-xenon collisions have also given interesting  
<sup>847</sup> complementary physics results.

<sup>848</sup> To accelerate protons to the design center-of-mass energy, a sequence of pre-accelerators  
<sup>849</sup> boosts the proton beams before injecting them into the next link. A schematic of the full  
<sup>850</sup> accelerator complex is presented in Fig. 5.1. Upon being produced and pre-collimated,  
<sup>851</sup> the protons are accelerated to 50 MeV in the Linac2, then to 1.4 GeV in the PS Booster,  
<sup>852</sup> to 26 GeV in the Proton Synchrotron (PS). Within the PS, the protons are collimated  
<sup>853</sup> into 25 ns-spaced (7.5 m) bunches of around  $1.15 \cdot 10^{11}$  protons per bunch. From there,  
<sup>854</sup> the Super Proton Synchrotron ramps up the energy to 450 GeV, and injects both beams  
<sup>855</sup> in opposite directions into the LHC itself. After approximately 20 minutes of acceleration  
<sup>856</sup> in the main LHC beampipe by 16 radiofrequency (RF) cavities, the proton bunches  
<sup>857</sup> achieve the current energy of 6.5 TeV per beam. From the start of Run II in 2015 until  
<sup>858</sup> the Long Shutdown of December 2018, the LHC delivered a total integrated luminosity  
<sup>859</sup> of around  $150 \text{ fb}^{-1}$  at a center-of-mass energy of 13 TeV and a peak luminosity of  
<sup>860</sup>  $2.1 \cdot 10^{34} \text{ cm}^{-2} \text{ s}^{-1}$ , even surpassing the design value.

<sup>861</sup> Equipped with 1232 superconducting main dipole magnets, the LHC operates with  
<sup>862</sup> magnetic fields of  $\sim 8.3$  T to keep the proton bunches on their circular trajectory. The  
<sup>863</sup> main dipoles are supplemented by higher-multipole magnets to correct for edge imper-  
<sup>864</sup> fections in the dipole field. Along the LHC lattice, 392 main quadrupole magnets are  
<sup>865</sup> used to re-focus the proton beams.

<sup>866</sup> Once at the nominal energy, the two circulating proton beams are made to collide  
<sup>867</sup> at four different interaction points, corresponding to the four biggest LHC experiments:

## 5 The LHC and the ATLAS detector

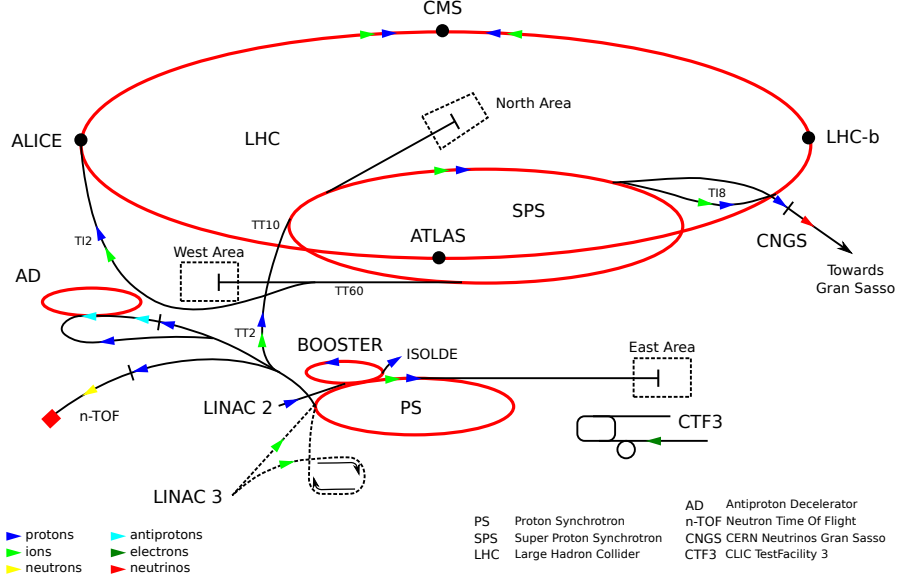


**Figure 5.1:** The LHC accelerator complex.

ATLAS, CMS, ALICE and LHCb. Out of these, ATLAS and CMS are general-purpose detectors designed to detect higher-mass particles like the Higgs boson or possible supersymmetric resonances, as well as to produce high-precision measurements of particles like the top-quark, whose properties were poorly resolved in earlier experiments. ALICE and LHCb, on the other hand, are dedicated to studies of heavy-ion collisions and focus on high-density QCD bound states and flavour physics. In the next Section, we will concentrate on the ATLAS detector substructure.

## 5.2 The ATLAS detector

A Toroidal LHC ApparatuS (ATLAS) aims for high-energy precision measurements of the SM in all possible sectors: with the help of the enormous statistics produced at LHC and the precision of the detector tracker and calorimeters, it allows for measurements of particle masses and couplings (from the CKM matrix to the Higgs boson coupling to other particles,  $\alpha_s$  measurements and PDF fits) or cross-section measurements, but also the observation of rare SM processes and decay channels (like  $t\bar{t}h$  production, light-by-light scattering or  $B^0 \rightarrow \mu^+\mu^-$  decays). These high-precision tests of the SM are intrinsically linked to searches for BSM physics: higher-scale BSM particles participating in loop corrections to the SM can have an important impact on the cross-sections or kinematic observables, and any observed deviation would hint at New Physics not far from the TeV scale. In general, though, direct searches are employed to discover potential high-mass resonances.

The ATLAS detector, situated at the LHC beam interaction point 1 near Meyrin, Switzerland, is an onion-shell structure comprised of particle trackers, an electromagnetic

and hadronic calorimeter, and a muon detector: from inner to outer radii, the produced particles encounter the Inner Detector, the Liquid Argon and the Tile Calorimeter, and finally the Muon Spectrometer. The detector itself is 44 m long and has a diameter of 25 m, and weighs more than 7000 tons. Fig. 5.2 shows a rendering of the ATLAS detector substructure. To bend the charged-particle tracks for momentum measurement, ATLAS relies on four magnets: a 2 T central solenoid close to the interaction point, an 8-coil barrel toroid that is cylindrically placed around the detector generating a magnetic field of 8 T, and two other 8-coil toroid magnets at the detector endcaps. The geometry of the magnet coils is shown in Fig. 5.3.

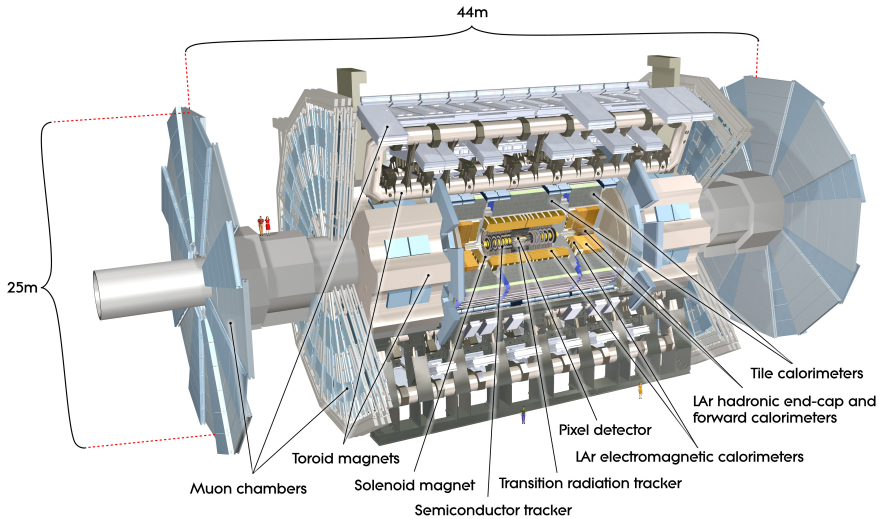


**Figure 5.2:** A cut-away view of the ATLAS detector.

By definition, the coordinate system is right-handed and centered at the interaction point, with the beam axis chosen as the  $z$ -axis, and the  $x$ -axis pointing towards the center of the LHC ring. The transverse plane is thus the  $(x, y)$ -plane.

### 5.2.1 The Inner Detector

Being the piece of equipment closer to the beampipe, the Inner Detector (ID) must fulfill several criteria for the reconstruction of charged-particles four-momenta, as well as for the identification of secondary vertices due to the decay of bottom-flavoured particles and the measurement of the impact parameter. The ID is further divided into a Silicon Pixel Detector (SPD), a Semiconductor Tracker (SCT) and a Transition Radiation Tracker (TRT). In Fig. 5.4, the structure of the ID is presented in a cut view along the beampipe (with the notable absence of the new insertable  $B$ -layer).

The SPD has a total of 86M channels and is the element closest to the interaction point. Four concentric layers of silicon pixel detectors are laid out around the beam axis in so-called barrel layers. The innermost layer is called the insertable  $B$ -layer (IBL) and was installed during the first Long Shutdown. It is only 3.3 cm away from the

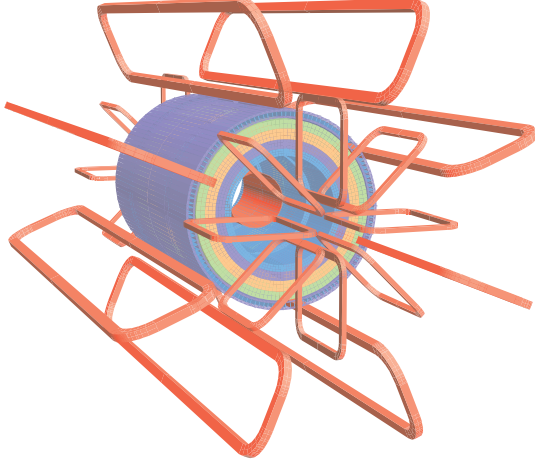
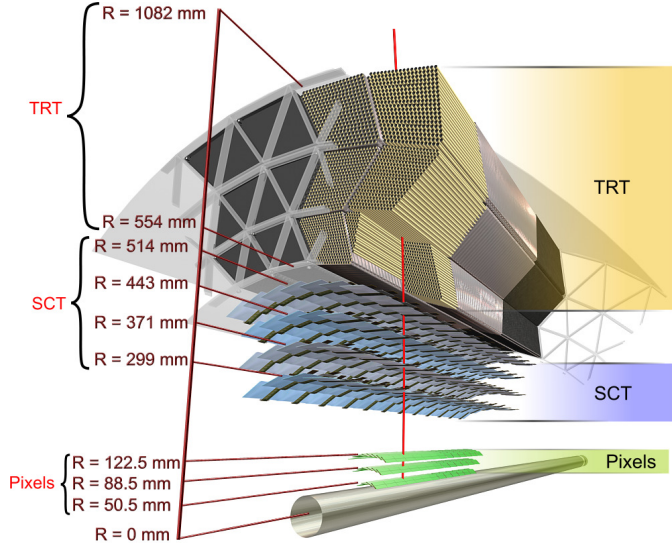


**Figure 5.3:** The geometry of the coils used to produce the magnetic field in the ATLAS detector. A solenoid magnet (4 T) is installed cylindrically around the beampipe, surrounded by a toroid magnet (8 T) and two endcap toroid magnets.

interaction point and allows for precise measurements of secondary vertex positions, and was designed to work in a high-radiation environment. Three other layers (including the earlier  $B$ -layer) are disposed concentrically around the beampipe, while three pixel disks are mounted on each endcap. All in all, the barrel layer and end-cap disks have a resolution of  $12\ \mu\text{m} \times 87\ \mu\text{m}$ , respectively  $13\ \mu\text{m} \times 78\ \mu\text{m}$  in the transverse-, respectively longitudinal- ( $T, L$ ) directions.

At intermediate radius, the SCT is a silicon microstrip tracker and provides, out of 6.2M readout channels, a measurement of the  $(\phi, r, z)$  track points. Four SCT barrel layers are disposed at radii between 299 mm and 514 mm away from the beampipe, while 18 more planar discs are placed at the endcaps. The barrel modules have a resolution of  $15\ \mu\text{m} \times 530\ \mu\text{m}$ .

Finally, at the outer layer, the TRTs are made of thin-walled straw tubes and give information for distinguishing between electrons and pions, as well as contribute to the transversal position measurement for a total of 350K readout channels. A straw tube is a 4 mm-diameter cylinder filled with gaseous xenon and a gold-plated tungsten wire strung through the middle. With the inner tube wall (cathode) and the wire (anode) held at 1.5kV of voltage difference, a charged particle passing through ionizes the gas, and the freed electrons drift to the wire: the drift time can then be used to determine the distance from the anode. Moreover, electron identification succeeds by the creation of transition-radiation photons created between the straws and converted in the xenon gas. The probability of transition radiation is proportional to the relativistic factor  $\gamma$ , which is usually higher for electrons and positrons. The TRTs determine the transversal position at a resolution of  $\sim 100\ \mu\text{m}$ .

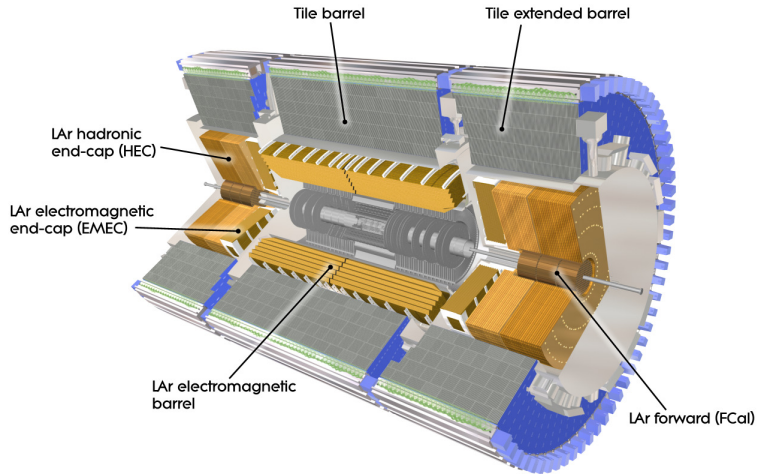


**Figure 5.4:** In order of increasing distance to the beampipe, the Inner Detector particle tracker is made up of the Silicon Pixel Detector, the microstrip Semiconductor Tracker (SCT), and the Transition Radiation Tracker (TRT).

### 937 5.2.2 The Liquid Argon (LAr) Calorimeter

938 Both the electromagnetic (EM) and the hadronic calorimeters are found between the  
 939 ID and the muon spectrometer. Fig. 5.5 depicts the LAr calorimeter in yellow, which  
 940 is closest to the ID and enveloped by the Tile Calorimeter (see Section 5.2.3). The  
 941 calorimeters mainly measure the energy deposited by the corresponding particle type,  
 942 but they also contribute to position measurements and particle identification (as well  
 943 as to the measurement of the missing transverse energy). The LAr calorimeter contains  
 944 both EM and hadronic detectors. In principle, a passing electron or photon produces  
 945 an electromagnetic shower in the EM calorimeter mainly through brehmsstrahlung and  
 946 electron-positron pair creation. In comparison, hadrons generate further hadronic ac-  
 947 tivity by primary nuclear reactions and spallation, as well as EM showers when the  
 948 produced particles decay electromagnetically. The LAr calorimeter functions as a sys-  
 949 tem of alternating lead/stainless steel absorbers and electrodes measuring the signal  
 950 drift-time, with the whole system immersed in liquid argon which plays the role of a  
 951 scintillator.

952 The electromagnetic barrel (EMB,  $|\eta| < 1.475$ ) and endcap (EMEC,  $1.375 < |\eta| < 3.2$ )  
 953 calorimeters use the same absorber material and geometry. In the forward region (FCal)  
 954 at rapidities  $3.1 < |\eta| < 4.9$ , a copper-based absorber covers EM activity while a tungsten  
 955 module provides measurement of hadronic energy deposition. Finally, a hadronic LAr  
 956 calorimeter is also placed at the endcaps (HEC) and should complement readings from  
 957 the Tile Calorimeter.

958 **5.2.3 The Tile Calorimeter (TileCal)**

**Figure 5.5:** The ATLAS calorimetry system is composed of the inner Liquid Argon calorimeter (yellow) and the outer Tile Calorimeter (gray).

959 The central and two extended barrel regions are covered by the TileCal, which is  
 960 cylindrically disposed around the beampipe (see Fig. 5.5) and is made of iron plate  
 961 absorbers and plastic scintillators as the active medium. The scintillating light created  
 962 by hadronic energy deposition is wavelength-shifted and led to photomultiplier tubes  
 963 that amplify the signal.

964 **5.2.4 The Muon Spectrometer**

965 At the outmost layer of the ATLAS detector, the Muon Spectrometer (MS) is designed  
 966 to deliver high-precision measurements of the muons' transverse momentum. It uses  
 967 four different techniques to trigger and detect the produced muons: the resistive-plate  
 968 chambers (RPC), cathode strip chambers (CSC), monitored drift tubes (MDT) and thin-  
 969 gap chambers (TGC), shown in Fig. 5.6. The muons are bent by three toroid magnets  
 970 which contain the detectors, for a rapidity-dependent magnetic field of  $0.3 - 1.2$  T which  
 971 amounts to a resolution of  $\sim 10\%$  in the transverse momentum of high-energy muons at  
 972 around 1 TeV. Both the RPCs and the TGCs are used as a first-level trigger on well-  
 973 resolved, high- $p_T$  muons in the barrel region, respectively the endcaps. On the other  
 974 hand, the MDTs which are laid out in the barrel and endcap regions, and the CSCs in  
 975 the forward region, measure the position of the incoming muons in the bending plane.

976 **5.2.5 Trigger & Data acquisition**

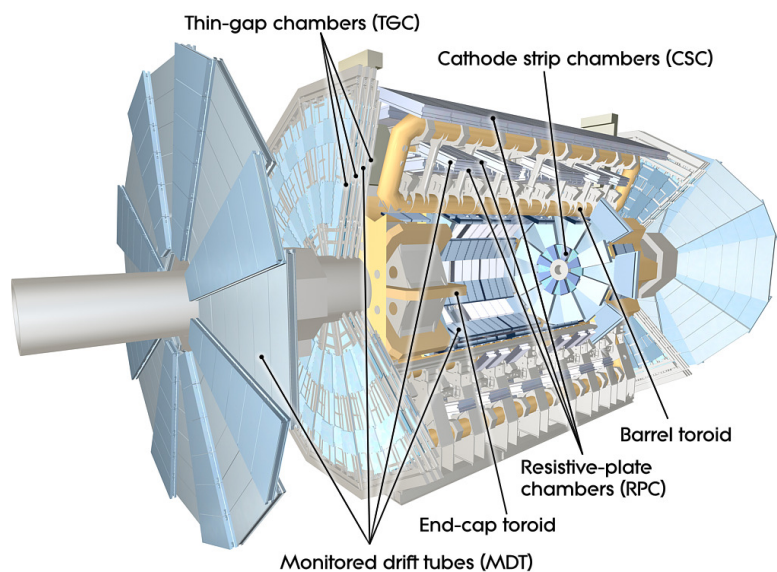


**Figure 5.6:** The ATLAS muon spectrometer.



## 977 6 Theoretical predictions for $t\bar{t}$ final-states

978 The top-quark pairs created e.g. at the LHC are not observable *per se*. The only directly  
 979 measurable quantities are the kinematic properties of the decayed final-states. Fortunately,  
 980 the top-quark has a branching ratio of 99.8% for  $t \rightarrow W^+ b$ ,  $\bar{t} \rightarrow W^- \bar{b}$ . So, the  
 981 final-state contains two  $b$ -jets that can be experimentally tagged, and depends only on the  
 982 decay mode of the  $W$  boson. In the case of top-quark pair production, both  $W$ -bosons  
 983 can decay either hadronically or leptonically, with branching ratios  $\Gamma(W \rightarrow q\bar{q}') = 0.67$ ,  
 984  $\Gamma(W \rightarrow \ell\nu_\ell) = 0.33$ : so the final-state can either be dileptonic, monoleptonic (lepto-  
 985 ton+jets) or all-hadronic, and the top-quark properties must then be reconstructed from  
 986 the measured final-states. Fig. 6.1 depicts the topology of the three decay channels and  
 987 Table 6.1 gives an overview of their respective cross-sections, advantages and disadvantages.  
 988

989 A precise computation for top-quark pair production cross-section and differential  
 990 observables is of paramount importance for the extraction of top-quark properties. Most  
 991 theoretical systematic uncertainties are well under control and have been the subject of  
 992 various studies in the last few years. In this Chapter, we first review the different  
 993 theoretical descriptions of  $pp \rightarrow t\bar{t}$  production, summarize the most important issues  
 994 and discuss their potential impact on the extraction of top-quark properties from data,  
 995 with a special focus on the top-quark observables. To do so in a realistic and quantitative  
 996 way, we setup an analysis close to the ATLAS 8 TeV top-quark mass extraction in the  
 997 dilepton channel. The dilepton channel is the cleanest decay mode for an experimental  
 998 measurement of the top-quark mass. It has the advantage of having a small background  
 999 (coming mainly from fake leptons, diboson and  $Z$ +jets production) and a clean signature,

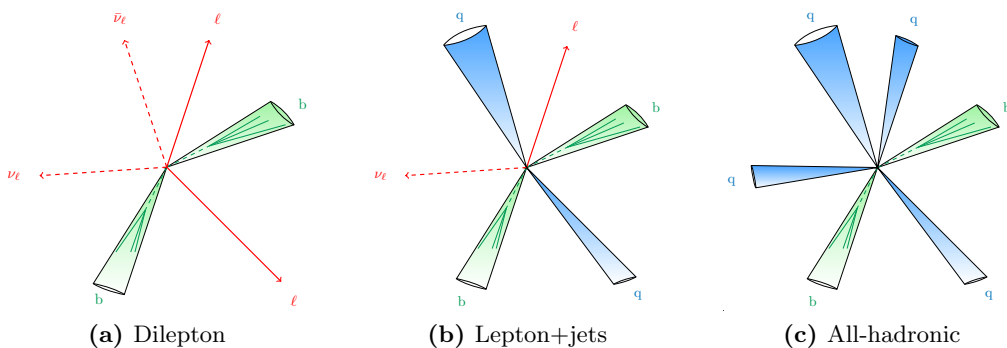


**Figure 6.1:** Topologies for  $t\bar{t}$  events are either stemming from (a) dileptonic, (b) monoleptonic or (c) all-hadronic decays.

## 6 Theoretical predictions for $t\bar{t}$ final-states

Final-state $X$	dilepton (w. $\tau^+\tau^-$ )	$\ell+$ jets (w. $\tau+j$ )	all-hadronic	all channels
$\Gamma(t\bar{t} \rightarrow X) [\%]$	10.89	44.02	44.89	100.0
$\sigma_{\text{NNLO}} [\text{pb}]$	90.58	366.14	373.38	$831.76^{+2.37\%}_{-3.51\%}$
Advantages	Clean signature	Full reconstruction	Largest branching	
Drawbacks	No full reconstruction	Jet-scale uncertainties	QCD background	
References	[61, 62, 63], [64, 65]	[62, 66], [67]	[68], [69]	

**Table 6.1:** For the three decay channels in  $t\bar{t}$  production, the branching ratios and inclusive theoretical cross-sections at QCD NNLO were computed with the Top++ program [70] for a top-quark mass  $m_t = 172.5$  GeV. Advantages and drawbacks of (any) top-quark measurement in said channel are given. References for ATLAS measurements of the top-quark mass in particular are also laid out for each subchannel for the top-quark pole mass (in black), and for the MC mass (in blue) from template fits.

1000 but suffers from the small branching fraction ( $\Gamma \sim 4.9\%$  for  $e/\mu$  in the final-state). Cross-  
1001 sections for all considered theoretical descriptions of  $t\bar{t}$  final-states are given at the end  
1002 of the Chapter for the ATLAS 13 TeV cuts.

### 1003 6.1 The narrow-width approximation

1004 If we consider the intermediate state  $W^+W^-b\bar{b}$ , it makes sense at first to approximate  
1005 it and examine only on-shell, doubly-resonant diagrams: the cross-section contribution  
1006 stemming from non-resonant diagrams is expected to be of the order of  $\mathcal{O}(\Gamma_t/m_t) \leq 1\%$ ,  
1007 and usually neglecting other contributions is fine. This description is called the *narrow-*  
1008 *width approximation* (NWA), and it builds on the limit  $\Gamma_t \rightarrow 0$ , where the top-quark  
1009 propagator can then be written as

$$\lim_{\Gamma_t \rightarrow 0} \frac{1}{(p^2 - m_t^2) + m_t^2 \Gamma_t^2} = \frac{\pi}{m_t \Gamma_t} \delta(p^2 - m_t^2) + \mathcal{O}\left(\frac{\Gamma_t}{m_t}\right) \quad (6.1)$$

1010 That is, top-quark production and decay entirely factorize, i.e.:

$$\mathcal{M}_{pp \rightarrow W^+W^-b\bar{b}} = \mathcal{M}_{pp \rightarrow t\bar{t} \rightarrow W^+W^-b\bar{b}}^{\text{NWA}} + \mathcal{O}(\Gamma_t/m_t) \quad (6.2)$$

$$= \mathcal{P}_{pp \rightarrow t\bar{t}} \otimes \mathcal{D}_{t \rightarrow W^+b} \otimes \mathcal{D}_{\bar{t} \rightarrow W^-\bar{b}} + \mathcal{O}(\Gamma_t/m_t) \quad (6.3)$$

1011 where  $\mathcal{P}$  denotes the  $t\bar{t}$  production and  $\mathcal{D}$  the top-quark decay dynamics, and the  
1012 spin correlations are correctly taken into account as indicated by the symbol  $\otimes$ . The  
1013 corresponding three LO Feynman diagrams, as well as a few examples of one-loop dia-  
1014 grams for  $gg \rightarrow t\bar{t}$  production, are shown in Fig. 6.2. Nowadays, most of the theoretical  
1015 predictions used for the extraction of top-quark properties in experimental analyses rely  
1016 on NLO matrix-elements for top-quark pair production. The top-quark decay and all  
1017 subsequent radiation is left to the Monte-Carlo generator, with the approximations it  
1018 entails: particle decay usually only has LO accuracy, spin correlations (in particular in

## 6.1 The narrow-width approximation

the parton-shower) were only recently implemented, and resummation is as good as the shower algorithm's accuracy. Even so, there exists a number of more complete Monte-Carlo implementations for  $t\bar{t}$  production in the NWA: the effects of NLO corrections to both production and decay were investigated in the POWHEG-BOX-v2 [71, 72, 73] framework called `ttb_NLO_dec` [74]. The HERWIG 7.1 MC generator supports a new multijet merging algorithm adapted to  $t\bar{t}$  production at NLO, and finally the SHERPA generator allows for the matching of the CS shower to  $t\bar{t}$  production with 1-, 2- and 3-jets at NLO.

Furthermore, some dedicated calculations have appeared over the years. In particular, QCD NNLO corrections for  $t\bar{t}$  production have been calculated for differential distributions [75, 76, 77], and combined with NLO EW corrections [78]. For a review of NLO EW effects, see Refs. [79, 80, 81]. Leaving corrections in top-quark pair production and considering now the top-quark decay, it was later shown that higher-order corrections to the top-quark decay have a measurable impact on differential distributions in certain regions of phase-space. NLO radiative corrections to the top-quark decays were computed [82, 83, 84] and completed by NNLO QCD corrections [85, 86], NNLL resummation and other improvements above higher-order corrections in  $\alpha_s$  [87, 88, 89, 90, 91, 92]. Within the NWA, the calculation of QCD NNLO + NNLL' (soft-gluon and small-mass resummation) corrections for differential distributions was combined with NLO EW corrections and is the most complete fixed-order calculation up-to-date [93].

For the results shown in Section 6.5 in the NWA, the top-quark pair production is described at NLO QCD and factorizes from the top-quark decay. Furthermore, we consider only the  $e\mu$  dilepton channel, that is  $pp \rightarrow (e^+\nu_e)(\mu^-\bar{\nu}_\mu)b\bar{b}$  production for the analysis presented in Chapter 7. The accuracy for the top-quark decay is handled in three different ways.

- (1) Top-quark decay at LO is realized in the basic SHERPA setup, as in Ref. [94] (referred to as **NLO<sub>NWA</sub><sup>LOdec</sup>** from now on).
- (2) The top-quark decay at NLO is computed in Ref. [83], and is shortly described below (**NLO<sub>NWA</sub><sup>NLOdec</sup>**).
- (3) The top-quark decay is handled by the parton-shower, namely through the SHERPA CSS shower (**NLO<sub>PS</sub>**).

Briefly, the **NLO<sub>NWA</sub><sup>NLOdec</sup>** calculation in the NWA bases on the following formula where top-quark pair production and decay factorize. Taking the perturbative expansion of Eq. (6.3) to NLO gives

$$\begin{aligned} \mathcal{M}_{ij \rightarrow t\bar{t} \rightarrow b\bar{b}2\ell2\nu}^{\text{NWA, NLO}} = & \mathcal{P}_{ij \rightarrow t\bar{t}}^{\text{LO}} \otimes \mathcal{D}_{t \rightarrow b\ell^+\nu}^{\text{LO}} \otimes \mathcal{D}_{\bar{t} \rightarrow \bar{b}\ell^-\bar{\nu}}^{\text{LO}} + \mathcal{P}_{ij \rightarrow t\bar{t}}^{\delta\text{NLO}} \otimes \mathcal{D}_{t \rightarrow b\ell^+\nu}^{\text{LO}} \otimes \mathcal{D}_{\bar{t} \rightarrow \bar{b}\ell^-\bar{\nu}}^{\text{LO}} \\ & + \mathcal{P}_{ij \rightarrow t\bar{t}}^{\text{LO}} \otimes \left( \mathcal{D}_{t \rightarrow b\ell^+\nu}^{\delta\text{NLO}} \otimes \mathcal{D}_{\bar{t} \rightarrow \bar{b}\ell^-\bar{\nu}}^{\text{LO}} + \mathcal{D}_{t \rightarrow b\ell^+\nu}^{\text{LO}} \otimes \mathcal{D}_{\bar{t} \rightarrow \bar{b}\ell^-\bar{\nu}}^{\delta\text{NLO}} \right). \end{aligned} \quad (6.4)$$

As mentioned above, the NWA is expected to be precise enough for most calculations and yet, NLO and off-shell effects in the top-quark decay can have an important impact

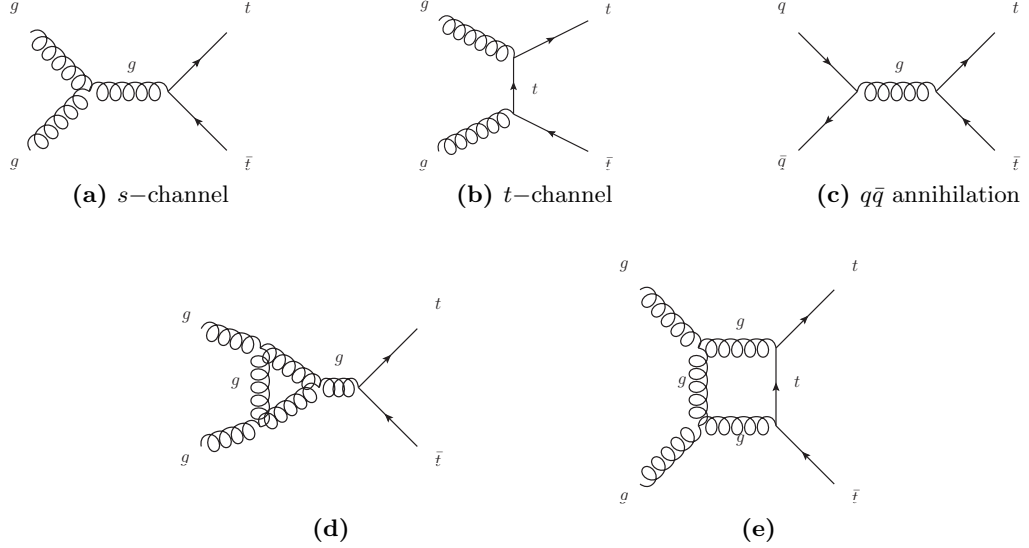


**Figure 6.2:** (a-c) Leading-order diagrams for  $t\bar{t}$  production and (d-e) two examples of NLO QCD one-loop diagrams for  $gg \rightarrow t\bar{t}$

1055 on sensitive regions of phase-space. In practice, analyses either include single-top quark  
 1056 production in the signal, or have to subtract it consistently as background since it  
 1057 contributes to the same final-state at NLO. This is generally accomplished with the  
 1058 help of a diagram subtraction (DS) or diagram removal (DR) scheme [95] to account for  
 1059 the interference between top-quark pair and single-top production. This procedure is  
 1060 not entirely free of quirks and violates gauge-invariance. To get an entirely consistent  
 1061 theoretical prediction, it is therefore preferable to produce the full intermediate state  
 1062  $pp \rightarrow W^+W^-b\bar{b}$ , which contains the complete set of Feynman diagrams at NLO.

## 1063 **6.2 $W^+W^-b\bar{b}$ production at NLO QCD**

1064 In this Section, we shall describe the setup used for calculating NLO QCD corrections to  
 1065 the  $pp \rightarrow W^+W^-b\bar{b}$  process, which is computationally more demanding than  $t\bar{t}$  produc-  
 1066 tion in the NWA. The full calculation at NLO contains all doubly-resonant top-quark  
 1067 diagrams, but also non-doubly resonant as well as non-factorizing contributions. Fig. 6.3  
 1068 illustrates the additional Feynman diagrams.

1069 At LO, the full  $W^+W^-b\bar{b}$  final-state including the non-resonant diagrams had been  
 1070 computed in Refs. [96, 97, 98, 94]. In general, the calculation of NLO corrections poses  
 1071 some technical problems because of the existence of  $b$ -quarks in both initial- and final-  
 1072 state. In the 5-flavour scheme (5FNS), where  $b$ -quarks are treated as massless, collinear  
 1073  $g \rightarrow b\bar{b}$  splittings contribute to the final-state and the corresponding IR divergence  
 1074 has to be handled (see Section 6.3). Considering massive  $b$ -quarks (4FNS) has the  
 1075 advantage of allowing any phase space restrictions on the  $b$ -quarks without endangering

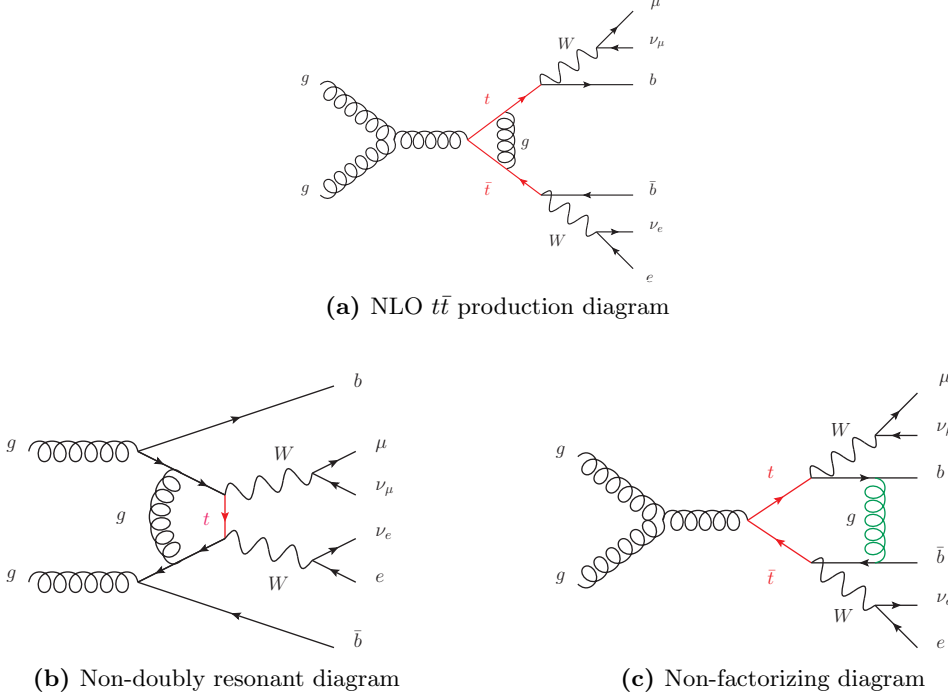


**Figure 6.3:** One-loop diagrams for  $pp \rightarrow W^+W^-b\bar{b}$  production contain (a) NLO corrections to standard NWA  $t\bar{t}$  production, but also (b) diagrams with one or no top-quark propagators and (c) resonant diagrams with non-factorizing legs

infrared safety, and thus allows to consider exclusive 0, 1- and 2-jet bins for  $pp \rightarrow (e^+\nu_e)(\mu^-\bar{\nu}_\mu)b\bar{b}$  in the same setup. On the other hand, massive  $b$ -quarks are accompanied by an additional mass scale to the one-loop integrals and thus renders the integral evaluation less straightforward. In Refs. [99, 100], NLO calculations in the 4FNS have been performed.

Often, the  $W^+W^-b\bar{b}$  prediction differs from the NWA in phase-space regions accessible only at NLO or sensitive to the top-quark decay kinematics. In Ref. [94], particular emphasis has been put on the impact of the non-factorising contributions on the top quark mass measurements in the dilepton channel. Recently the calculation of the NLO QCD corrections to  $W^+W^-b\bar{b}$  production with full off-shell effects has also been achieved in the lepton+jets channel [101].

## 6.3 Calculation setup

The calculation is analogous to the one described in Ref. [102]. We compute the NLO QCD corrections to the  $pp \rightarrow W^+W^-b\bar{b} \rightarrow (e^+\nu_e)(\mu^-\bar{\nu}_\mu)b\bar{b}$  process, i.e. up to  $\mathcal{O}(\alpha_s^2\alpha^2)$ , in the 5-flavour scheme. This means that interference from (massless)  $b$ -quarks in the initial-state is taken into account. Top-quark finite width effects are fully included. The

## 6 Theoretical predictions for $t\bar{t}$ final-states

1092 complex mass scheme is used to incorporate the width in a gauge-invariant way, where  
 1093 the top-quark mass is replaced by a complex number  $\mu_t$ :

$$\mu_t^2 = m_t^2 - im_t\Gamma_t. \quad (6.5)$$

1094 The  $W$ - and intermediate  $Z$ -bosons also acquire a complex mass. Note that we con-  
 1095 sider only resonant  $W$ -boson diagrams: non-resonant contributions and finite- $W$ -width  
 1096 effects were found to be small compared to top-quark effects [103]. The calculation is  
 1097 realized at parton-level within the SHERPA v2.2.3 framework, where we used tree-level  
 1098 and real amplitudes from SHERPA matrix-element generators COMIX and AMEGIC. The  
 1099 one-loop amplitudes are compiled by GoSAM and linked to SHERPA via the BLHA  
 1100 interface. Finally, the IR divergences are subtracted with the help of the Catani-Seymour  
 1101 dipole formalism as automated in SHERPA.

1102 There are 334 diagrams contributing to the  $q\bar{q} \rightarrow W^+W^-b\bar{b}$  virtual corrections, where  
 1103  $q$  are the light quarks  $u, d, s, c$ , and 1068 diagrams to  $gg \rightarrow W^+W^-b\bar{b}$ . Additionally,  
 1104 because of the  $b$ -quarks present in the initial-state, 668 one-loop diagrams contribute  
 1105 to  $b\bar{b} \rightarrow W^+W^-b\bar{b}$ .

1106 In the results presented in Chapters 7 and 8, the full  $pp \rightarrow W^+W^-b\bar{b} \rightarrow (e^+\nu_e)(\mu^-\bar{\nu}_\mu)b\bar{b}$   
 1107 QCD NLO prediction is compared with various  $t\bar{t}$  predictions in the NWA. To disen-  
 1108 tangle the effects from production and decay corrections (as well as extra radiation in  
 1109 a parton-shower resummed approximation), the four theoretical descriptions considered  
 1110 in the next Chapter are summarized again for completeness:

- 1111     **NLO<sub>full</sub>**: full NLO corrections to  $pp \rightarrow W^+W^-b\bar{b}$  with leptonic  $W$ -decays,
- 1112     **NLO<sub>NWA</sub><sup>NLOdec</sup>**: NLO  $t\bar{t}$  production  $\otimes$  NLO decay,
- 1113     **NLO<sub>NWA</sub><sup>LOdec</sup>**: NLO  $t\bar{t}$  production  $\otimes$  LO decay,
- 1114     **NLO<sub>PS</sub>**: NLO  $t\bar{t}$  production+shower  $\otimes$  decay via parton showering.

1115 The PDF4LHC15\_nlo\_30\_pdfas sets are interfaced to SHERPA via LHAPDF and events  
 1116 are produced at a centre-of-mass energy of  $\sqrt{s} = 13$  TeV. The central top-quark mass  
 1117 was set to  $m_t = 172.5$  GeV and the  $G_\mu$ -electroweak scheme was used with the following  
 1118 numerical values:

$$G_\mu = 1.16637 \cdot 10^{-5} \text{ GeV}^{-2}, \quad M_W = 80.385 \text{ GeV}, \quad M_Z = 91.1876 \text{ GeV}, \quad (6.6)$$

$$\begin{aligned} \Gamma_t^{\text{LO}} &= & 1.4806 \text{ GeV}, & \Gamma_t^{\text{NLO}} &= & 1.3535 \text{ GeV}, \\ \Gamma_W^{\text{LO}} &= & 2.0454 \text{ GeV}, & \Gamma_W^{\text{NLO}} &= & 2.1155 \text{ GeV}, \\ \Gamma_Z &= & 2.4952 \text{ GeV}, & & & \end{aligned} \quad (6.7)$$

1119 where the LO (NLO) widths were used for the LO (NLO) decays, respectively.

## 6.4 Event requirements

To give a more quantitative assessment of the difference between our predictions with respect to the extracted top-quark mass, we implement an analysis that is similar to the ATLAS top-quark mass measurement in the dilepton channel at 8 TeV [104], where the trigger cuts on leptons and jets are adapted to the ATLAS 13 TeV standards. For details of the analysis, the reader is referred to Chapter 7. We require:

- $n_{b,\text{jet}} = 2$  with  $p_T^{\text{jet}} > 25 \text{ GeV}$  and  $|\eta^{\text{jet}}| < 2.5$ . Jets containing a  $b\bar{b}$  pair are also defined as  $b$ -jets.
- exactly two oppositely charged leptons which fulfill  $p_T^\mu > 28 \text{ GeV}$ ,  $|\eta^\mu| < 2.5$  for muons and  $p_T^e > 28 \text{ GeV}$ ,  $|\eta^e| < 2.47$  for electrons excluding the dead region  $1.37 < |\eta^e| < 1.52$  between barrel and endcap EM calorimeters. For charged leptons we require a separation of  $\Delta R(\ell, \text{jet}) > 0.4$  to any jet.
- $p_T^{lb} > 120 \text{ GeV}$ . Using the same lepton- $b$ -jet assignments as for  $m_{lb}$ , we define  $p_T^{lb}$  as the average transverse momentum of both lepton- $b$ -jet systems.

We chose  $\mu_R = \mu_F = m_t$  as our central scale. The scale variation bands are obtained by varying  $\mu_{R,F} = c_{R,F} m_t$ , with  $(c_R, c_F) \in \{(0.5, 0.5), (2, 2)\}$ .<sup>1</sup>

In the NWA parton-shower results, the central scale was also compared to a dynamic scale called  $\mu_{t\bar{t}}$ . The latter is a “colour-flow inspired” QCD scale suggested in Ref. [105]. For the Mandelstam invariants  $s$ ,  $t$  and  $u$ , the dynamic scale is given by

$$\mu_{t\bar{t}}^2(q\bar{q} \rightarrow t\bar{t}) = 2 p_q p_t = m_t^2 - t , \quad (6.8)$$

$$\mu_{t\bar{t}}^2(\bar{q}q \rightarrow t\bar{t}) = 2 p_{\bar{q}} p_t = m_t^2 - u , \quad (6.9)$$

$$\mu_{t\bar{t}}^2(gg \rightarrow t\bar{t}) = \begin{cases} m_t^2 - t & \text{with weight } w_1 \propto \frac{u-m_t^2}{t-m_t^2} + \frac{m_t^2}{m_t^2-t} \left\{ \frac{4t}{t-m_t^2} + \frac{m_t^2}{s} \right\} \\ m_t^2 - u & \text{with weight } w_2 \propto \frac{t-m_t^2}{u-m_t^2} + \frac{m_t^2}{m_t^2-u} \left\{ \frac{4u}{u-m_t^2} + \frac{m_t^2}{s} \right\} . \end{cases} \quad (6.10)$$

the value of  $\mu_{t\bar{t}}$  being chosen with a probability proportional to the two weights  $w_1$ ,  $w_2$ .

## 6.5 Total cross-section results

The fiducial cross-sections after applying the cuts detailed above are given in Table 6.2 for all considered predictions, where we also add production at LO accuracy for completeness. The renormalization and factorization scale uncertainties are given in percent.

---

<sup>1</sup>Also, 7-point variations were considered but the simultaneous variations are identical to their envelope.

	X=LO [fb]	X=NLO [fb]
<b>X<sub>full</sub></b>	$(739.5 \pm 0.3)^{+31.5\%}_{-22.4\%}$	$(914 \pm 3)^{+2.1\%}_{-7.6\%}$
<b>X<sub>NWA</sub><sup>LOdec</sup></b>	$(727.3 \pm 0.2)^{+31.4\%}_{-22.3\%}$	$(1029 \pm 1)^{+10.4\%}_{-11.5\%}$
<b>X<sub>NWA</sub><sup>NLOdec</sup></b>	-	$(905 \pm 1)^{+2.3\%}_{-7.7\%}$
<b>X<sub>PS</sub>, <math>\mu = m_t</math></b>	$(637.7 \pm 0.9)^{+29.7\%}_{-21.0\%}$	$(886 \pm 1)^{+8.5\%}_{-9.3\%}$
<b>X<sub>PS</sub>, <math>\mu = \mu_{t\bar{t}}</math></b>	$(499.7 \pm 0.7)^{+27.6\%}_{-19.3\%}$	$(805.2 \pm 0.9)^{+12.3\%}_{-10.9\%}$

**Table 6.2:** Cross-sections for all predictions at LO, respectively NLO in production, where the top-quark mass  $m_t = 172.5$  GeV. The uncertainty stemming from MC integration is given in parentheses, and scale variation uncertainties are shown in percent.

# 1141 7 NWA versus $WWbb$ : Top-quark mass 1142 uncertainties at parton-level

1143 Because we base our extraction of the top-quark mass on the ATLAS 8 TeV analysis in  
1144 the dilepton channel, this Chapter first introduces the template fit method that was used  
1145 in the experimental measurement. After a short discussion of important features of the  
1146 considered observables, the results for the fit of the top-quark mass and its dependence  
1147 on the different theoretical descriptions of the  $t\bar{t}$  dilepton final-state are laid out.

## 1148 7.1 The template fit method

1149 In the dilepton channel, the top-quark momenta cannot be fully reconstructed because  
1150 of the two-particle spectrum spread given by the neutrinos from both  $W$ -decays. One  
1151 successful method is to use a differential distribution that is sensitive to the top-quark  
1152 mass instead and which can be defined without having to properly reconstruct the top-  
1153 quarks. The procedure is the following:

- 1154 • Choose a distribution that is sensitive to the theoretical top-quark mass: for ex-  
1155 ample, we choose the average invariant mass of the lepton- $b$ -jet system  $m_{\ell b}$  as a  
1156 function of the top-quark mass set in the MC event generator.
- 1157 • Generate distributions for different input top-quark masses  $m_t^{\text{in}}$ . In Fig. 7.2, the  
1158 dependence of  $m_{\ell b}$  on the MC generator input top-quark mass is illustrated, as  
1159 well as three other potential candidate observables.
- 1160 • Individually fit the distributions simulated for the input masses  $m_t^{\text{in}}$  with an ap-  
1161 propriate function. If we consider the simple example of a Gaussian fit, this gives:

$$\mathcal{G}(A, \mu, \sigma; m_t^{\text{in}}) = A(m_t^{\text{in}}) \exp\left(-\frac{\mu(m_t^{\text{in}}) - m_t^{\text{in}}}{2\sigma^2(m_t^{\text{in}})}\right), \quad (7.1)$$

1162 where the parameters  $A$ ,  $\mu$ ,  $\sigma$  are fit to the distributions generated for each input  
1163 mass.

1164 This step is called *calibration* in the following paragraphs, and the functions for each of  
1165 the input top-quark masses are called *templates*. The dependence of the parameters on  
1166  $m_t^{\text{in}}$  is assumed to be linear, a fact that is checked against the MC prediction. Once it is  
1167 confirmed, the linear dependence is imposed (in our example,  $A(m_t^{\text{in}}) = a + b \cdot m_t^{\text{in}}$  with  $a$   
1168 and  $b$  fixed, and analogously for  $\mu(m_t^{\text{in}})$ ,  $\sigma(m_t^{\text{in}})$ ). The underlying linear parameters are

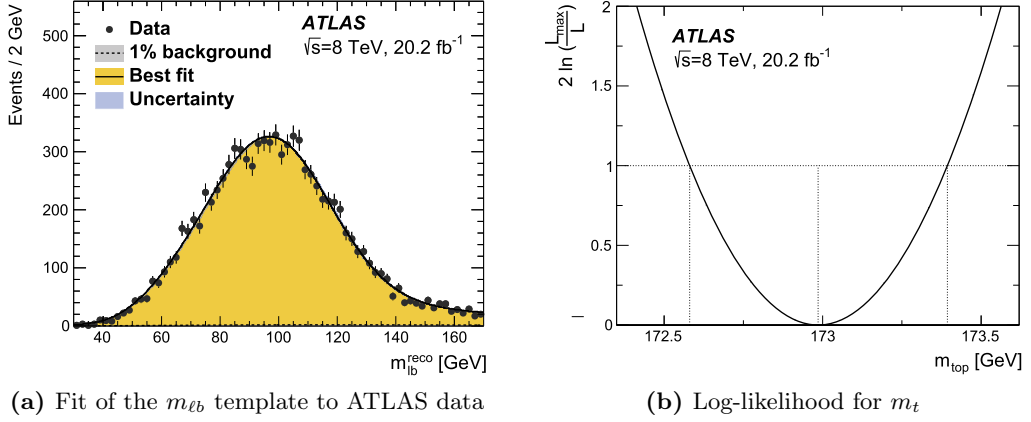


**Figure 7.1**

then kept constant, and the only floating parameter is the extracted top-quark mass  $m_t^{\text{out}}$  to be measured. This function can then be used directly in an unbinned likelihood fit to the distribution measured in experimental data, as shown in Fig. 7.1 as an illustration from the ATLAS 8 TeV measurement.

To correctly model the  $m_{lb}$  distribution, the sum of a Gaussian and a Landau distribution is used in the analysis. Also, the overall normalization factor is fit to the measured cross-section after cuts are applied. In the rest of this Chapter, we repeat the extraction from an analysis similar to the one performed by ATLAS, for the four different theoretical setups presented in Chapter 6 at parton-level (particle-level for the parton-showered  $t\bar{t}$  results). We also compare different observables in addition to  $m_{lb}$ .

## 7.2 Definition of the observables

We study a list of observables that should in principle be maximally sensitive to the top-quark mass while minimally sensitive to theoretical systematic uncertainties (that is, including differences between NWA and full  $W^+W^-b\bar{b}$  predictions):

- $m_{lb}$  – the invariant mass of the lepton- and  $b$ -jet system

$$m_{lb}^2 = (p_\ell + p_b)^2 \quad (7.2)$$

Since both top-quarks decay leptonically, and since there is no possibility to determine the charge of the  $b$ -jets experimentally, there is an ambiguity in the assignment of the lepton and  $b$ -jet to the two top-quarks. We use here the same criterion as the ATLAS analysis: the two possible pairs for the lepton- $b$ -jet system ( $\ell^+b_1, \ell^-b_2$ ) are tried out, and we choose the pairing that minimizes the sum of the two  $m_{lb}$  values per event. This gives a correct reconstruction in  $\sim 77\%$  of cases.

### 7.3 Comparison of the different theoretical descriptions

- $m_{T2}$  – following Refs. [106, 107] in the case of the final-state  $(e^+\nu_e)(\mu^-\bar{\nu}_\mu)b\bar{b}$ , the definition of this variable is given by

$$m_{T2}^2 = \min_{p_T^{\nu_1} + p_T^{\nu_2} = p_T^{\text{miss}}} \left[ \max \left\{ m_T^2 \left( p_T^{(\ell^+ b_1)}, p_T^{\nu_1} \right), m_T^2 \left( p_T^{(\ell^- b_2)}, p_T^{\nu_2} \right) \right\} \right]. \quad (7.3)$$

The same pairing as for  $m_{\ell b}$  is chosen for the lepton and b-jet systems, and the transverse mass is defined as

$$m_T^2 \left( p_T^{(\ell b_i)}, p_T^{\nu_i} \right) = m_{(\ell b_i)}^2 + 2 \left( E_T^{(\ell b_i)} E_T^{\nu_i} - p_T^{(\ell b_i)} p_T^{\nu_i} \right) \quad (7.4)$$

with  $E_T = \sqrt{|p_T|^2 + m^2}$  and we set  $m_{\nu_i} = 0$ .

- $E_T^{\Delta R}$  – the leptons' transverse energy weighted by the angular distance to the corresponding b-jet

$$E_T^{\Delta R} = \frac{1}{2} \left( E_T^{l_1} \Delta R(l_1, b_1) + E_T^{l_2} \Delta R(l_2, b_2) \right) \quad (7.5)$$

where again the above  $m_{\ell b}$  criterion is used.

Sets of MC samples were produced for input top-quark masses

$$m_t \in \{165 \text{ GeV}, 172.5 \text{ GeV}, 180 \text{ GeV}\}.$$

The dependence on the input top-quark mass  $m_t$  is shown for all four observables in Fig. 7.2. Whereas  $m_{\ell b}$  and  $m_{T2}$  are the most sensitive to  $m_t$  with a ratio of the order  $\mathcal{O}(2-3)$  for the considered masses, the dependence of the  $E_T^{\Delta R}$  and  $m_{\ell\ell}$  observables on the top-quark mass is rather weak.

## 7.3 Comparison of the different theoretical descriptions

The normalized differential cross-section for the  $m_{\ell b}$  observable is outlined in Fig. 7.3 for the four theoretical predictions presented in Chapter 6. We show the ratio to the complete  $W^+W^-b\bar{b}$  calculation, where the latter's scale uncertainties are represented by gray bands in the plot. Note that the  $m_{\ell b}$  distribution has a sharp kinematic edge at  $m_{\ell b}^{\text{edge}} = \sqrt{m_t^2 - m_W^2} \sim 153 \text{ GeV}$ . Beyond the kinematic edge, the bins are only populated by wrong lepton-b-jet pairing, additional radiation from the initial-state clustered along the lepton-b-jet system, and non-resonant contributions. The LO cross-section for  $t\bar{t}$  production is equal to zero in this phase-space region. Because NLO corrections represent the first non-trivial order contributing to this region, differences between the theoretical descriptions considered here are expected to be sizeable around and above this kinematic edge. On the other hand, as seen in Fig. 7.2, this region also displays the highest sensitivity to the top-quark mass. The template fit strategy should therefore